



Tomás Colaço Ribeiro Fernandes

Bachelor Degree in Micro and Nanotechnologies Engineering

Digital Fabrication of Transparent Electrodes for Simultaneously Optical and Electrochemical Biosensor Applications

Dissertation submitted in partial fulfillment of the requirements for the degree of
Master of Science in Micro and Nanotechnologies Engineering

Adviser: Dr. Elvira Fortunato, Full Professor, Faculty of Science and Technology, NOVA University of Lisbon

Co-adviser: Dr. Maria Goreti Sales, Adjunct Professor, School of Engineering of the Polytechnique School of Porto



FACULDADE DE
CIÊNCIAS E TECNOLOGIA
UNIVERSIDADE NOVA DE LISBOA

Setembro, 2018

Digital Fabrication of Transparent Electrodes for Simultaneously Optical and
Electrochemical Biosensor Applications

Digital Fabrication of Transparent Electrodes for Biosensor Applications Using Spectroelectrochemical Analysis

Copyright © Tomás Colaço Ribeiro Fernandes, Faculdade de Ciências e Tecnologia, Universidade Nova de Lisboa.

A Faculdade de Ciências e Tecnologia e a Universidade Nova de Lisboa têm o direito, perpétuo e sem limites geográficos, de arquivar e publicar esta dissertação através de exemplares impressos reproduzidos em papel ou de forma digital, ou por qualquer outro meio conhecido ou que venha a ser inventado, e de a divulgar através de repositórios científicos e de admitir a sua cópia e distribuição com objetivos educacionais ou de investigação, não comerciais, desde que seja dado crédito ao autor e editor.

“What’s past is prologue.” – William Shakespeare

Digital Fabrication of Transparent Electrodes for Simultaneously Optical and
Electrochemical Biosensor Applications

Acknowledgements

A realização desta dissertação marca o final de uma importante e árdua etapa da minha vida. Como tal, gostaria de agradecer a todos aqueles que contribuíram para a sua concretização. Muitos nomes ficarão por mencionar, porém o vosso apoio tem e terá sempre um apreço incondicional da minha parte e deixo-vos o meu mais sincero agradecimento.

Primeiramente, quero agradecer à minha instituição, a grande Faculdade de Ciências e Tecnologias da Universidade NOVA de Lisboa e ao departamento de Ciências dos Materiais por todas as aventuras e grande espírito académico ao longo destes cinco anos.

À minha orientadora, Professora Elvira Fortunato, pelo seu conhecimento, disponibilidade e excelentes condições de trabalho que proporcionou não só nesta fase, como também ao longo de todo o curso. Estendo este agradecimento ao Professor Rodrigo Martins, pela sua visão e dedicação na criação do curso de Engenharia de Micro e Nanotecnologias.

À minha coorientadora, Professora Goreti Sales, pelos seus conselhos, confiança e ajuda pela criação de financiamento.

À Dr. Manuela Frasco pela paciência, *brainstorm* e acompanhamento e a todo o grupo do BioMark pelos braços abertos com que me receberam, pela boa-disposição contagiante e suporte moral. Destaco também a Sara, a Rita e a Carla por tudo o que me ensinaram.

A toda a equipa do CENIMAT pelo trabalho excepcional que fazem. À Ana Samouco pelo acompanhamento inicial, amizade e resposta a todas as perguntas estapafúrdias. À Sofia Ferreira por toda a ajuda, orientação, horas de deposições e explicações. À Carolina Marques pelo seu apoio incessante, pelas inúmeras ideias e atenção. À Professora Rita Branquinho, por ter sido a melhor professora que tive, por ser sempre prestável e me ter aberto esta porta.

À minha família e amigos, pelo suporte, compreensão, motivação e amor. Aos amigos do cinema pelas conversas idiotas, aos amigos dos jogos tardios pelos momentos de relaxamento e aos amigos da praxe, por todos os escapes que me ofereceram. Ao Dimi, ao Gui, ao Miguel, ao Moura e aos meus afilhados.

À minha mãe, por ter dado tudo o que tinha para que o meu futuro fosse melhor e por fazê-lo sozinha, incansavelmente. Ao meu avô, que sempre se sacrificou por mim e foi o pai que nunca tive.

Finalmente, à Marta Pereira, por ter partilhado esta experiência comigo, por ser a minha melhor amiga, sempre paciente, compreensiva e o meu maior apoio.

Digital Fabrication of Transparent Electrodes for Simultaneously Optical and
Electrochemical Biosensor Applications

Resumo

Esta dissertação propõe um biossensor pioneiro para detecção de biomarcadores de cancro, que combina um reconhecimento eletroquímico e ótico na mesma análise, ao tirar partido da padronização de elétrodos transparentes e flexíveis a partir de escrita direta por laser. O biomarcador, o antigénio carcino-embriónico, é detetado por um material biomimético semelhante a um anticorpo. O sensor produzido sobre vidros de óxido de índio dopado com estanho (ITO) consiste num cristal fotónico composto por nanopartículas de sílica incorporado num filme de polipirrole molecularmente impresso, obtido através de eletropolimerização de pirrole na presença do biomarcador. A interação entre o biomarcador e o material sensor traduz-se em sinais eletroquímicos capazes de gerar dados quantitativos. Simultaneamente, desencadeia uma diferença na reflectância da matriz do filme sensor, permitindo também o estudo do sinal ótico. Assim, as características analíticas do biossensor foram estudadas por Espectroscopia de Impedância Eletroquímica e pela reflectância da estrutura opala do cristal fotónico, tendo apresentado resposta a concentrações fisiologicamente relevantes (entre 2.5 ng/mL e 10 ng/mL).

Este sensor foi construído num substrato de ITO como prova de conceito, sendo este o melhor óxido entre vários materiais condutores produzidos em substrato de vidro, mesmo que a primeira parte do trabalho se concentre na preparação de filmes finos de óxido de zinco dopado com alumínio através de *sputtering* de radiofrequências e no fabrico de elétrodos através de escrita direta por laser. Estes processos foram otimizados para a fabricação de óxidos altamente condutores e transparentes, capazes de, no futuro, substituir o ITO como componente principal na indústria de eletrónica transparente e flexível.

O dispositivo sensor desenvolvido demonstrou potenciais características em termos de alta sensibilidade, estabilidade e dupla detecção, que o podem vir a tornar uma solução portátil, mais simples e de baixo custo para a detecção de CEA no local de prestação de cuidados quando comparado a métodos imunológicos convencionais. Simultaneamente, poderá abrir novas portas para outras aplicações e melhorar as perspetivas em termos de diagnóstico precoce de doenças.

Palavras-chave: anticorpos plásticos; óxido de zinco dopado com alumínio; escrita direta por laser; sputtering de RF; biossensor; óxidos condutores transparentes, nanopartículas de sílica.

Digital Fabrication of Transparent Electrodes for Simultaneously Optical and
Electrochemical Biosensor Applications

Abstract

This dissertation proposes a pioneering biosensor for detecting cancer biomarkers that combines electrochemical and optical recognition in the same analyzing spot, by taking advantage of laser direct writing to pattern transparent and flexible electrodes. The biomarker, the carcinoembryonic antigen (CEA), is detected by an antibody-like biomimetic material as recognizing agent. The sensing film over indium tin oxide (ITO) coated glass substrate consisted of a molecularly imprinted layer of polypyrrole (PPy). The imprinted film is assembled on a three-dimensional photonic crystal composed of silica nanoparticles (NPs), allowing optical detection. The molecularly imprinted polymer was obtained through electropolymerization of pyrrole in the presence of the biomarker as template. The interaction between the biomarker and the sensing material produces electrochemical signals generating quantitative data. In addition, it triggers a difference in the reflectance of the sensing photonic film matrix. The analytical features of the biosensor were assessed in PBS buffer by electrochemical impedance spectroscopy (EIS) and by reflectance of the opal-based photonic crystal. The response of the proposed biosensor was in the range of physiological relevant levels of CEA (from 2.5 ng/mL to 10 ng/mL). This sensor was assembled on an ITO substrate as proof of concept, the best substrate among the several conductive material produced on glass support, even if the first part of the work focuses on the preparation of aluminum doped zinc oxide (AZO) thin films by RF sputtering and laser direct writing. These processes were optimized for the fabrication of a highly conductive and transparent oxide capable of replacing ITO in the future as a main component in most transparent and flexible electronics applications.

The developed sensing device showed promising features to become a much simpler, faster and low-cost point-of-care (POC) portable solution for the detection of CEA when compared to conventional immunoassay approaches, due to its high sensitivity, stability and dual detection method. At the same time, it may open new doors for other applications and foreseen improvement concerning the early diagnosis of diseases.

Keywords: plastic antibodies; Aluminum doped Zinc oxide; laser direct writing; RF sputtering; biosensor; transparent conductive oxides; silica nanoparticles.

Digital Fabrication of Transparent Electrodes for Simultaneously Optical and
Electrochemical Biosensor Applications

Abbreviations

(3-Aminopropyl)Triethoxylosilane	APTES
Aluminum Doped Zinc Oxide	AZO
Attenuated Total Reflectance	ATR
Carcinoembryonic Antigen.....	CEA
Counter Electrode	CE
Cyclic Voltammetry	CV
Electrochemical Impedance Spectroscopy	EIS
Enzyme-Linked Immunosorbent Assay	ELISA
Gas Chromatography-Mass Spectrometry	GCMS
High Performance Liquid Chromatography	HPLC
Indium Tin Oxide	ITO
Molecularly Imprinted Polymer.....	MIP
Nanoparticles	NPs
Photonic Crystals	Pcs
Point-Of-Care	POC
Polyethylene Naphthalate	PEN
Polyethylene Terephthalate	PET
Polypyrrole.....	Ppy
Pyrrrole	Py
Rapid Thermal Annealing	RTA
Reference Electrode	RE
Scanning Electron Microscopes	SEM
Solution Resistance	R_s
Tetraethyl Orthosilicate	TEOS
Transparent Conductive Oxide	TCO
Working Electrode	WE
X-Ray Diffraction	XRD

Digital Fabrication of Transparent Electrodes for Simultaneously Optical and
Electrochemical Biosensor Applications

Table of Contents

ACKNOWLEDGEMENTS.....	III
RESUMO.....	V
ABSTRACT	VII
ABBREVIATIONS	IX
TABLE OF CONTENTS	XI
LIST OF FIGURES.....	XIII
LIST OF TABLES.....	XV
MOTIVATION AND OBJECTIVES.....	XVI
1 INTRODUCTION.....	1
1.1 CANCER DIAGNOSIS.....	1
1.2 BIOSENSORS.....	2
1.2.1 <i>Optical Biosensors</i>	2
1.2.2 <i>Electrochemical Biosensors</i>	3
1.3 MOLECULARLY IMPRINTED POLYMERS	5
1.4 TRANSPARENT AND FLEXIBLE ELECTRONICS	6
2 MATERIALS AND METHODS.....	7
2.1 AZO THIN FILM DEPOSITION.....	7
2.1.1 <i>Physical Vapor Deposition – RF Sputtering</i>	7
2.1.2 <i>Rapid Thermal Annealing</i>	8
2.2 LASER DIRECT WRITING	8
2.2.1 <i>Apparatus</i>	8
2.2.2 <i>Thin Film Etching</i>	8
2.3 THIN FILMS CHARACTERIZATION	8
2.3.1 <i>X-Ray Diffraction</i>	8
2.3.2 <i>UV-Visible-NIR Transmittance Spectroscopy</i>	9
2.3.3 <i>Scanning Electron Microscopy</i>	9
2.3.4 <i>Four-Point-Probe Measurements</i>	9
2.3.5 <i>Hall-Effect Measurements</i>	9
2.3.6 <i>Contact Profilometry</i>	9
2.4 BIOSENSOR ASSAY	9
2.4.1 <i>Apparatus</i>	9
2.4.2 <i>Electrochemical Procedures</i>	10
2.5 SENSING MATERIAL ASSEMBLY	10
2.5.1 <i>Silica Nanoparticles Synthesis and Functionalization</i>	10

Digital Fabrication of Transparent Electrodes for Simultaneously Optical and
Electrochemical Biosensor Applications

2.5.2	<i>Nanoparticles Deposition</i>	11
2.5.3	<i>Molecularly Imprinted Photonic Sensor Construction</i>	11
2.6	BIOSENSOR CHARACTERIZATION	12
2.6.1	<i>Fourier-Transform Infrared Spectroscopy</i>	12
2.6.2	<i>Scanning Electron Microscopy</i>	12
2.6.3	<i>Analytical performance of the biosensor</i>	12
3	 RESULTS AND DISCUSSION	13
3.1	OPTIMIZATION, PRODUCTION AND CHARACTERIZATION OF TCO'S	13
3.1.1	<i>AZO Deposition Optimization</i>	13
3.1.2	<i>Laser Parameters – Glass Substrates</i>	18
3.1.3	<i>Laser Parameters – Flexible Substrates</i>	20
3.1.4	<i>ITO Electrodes</i>	20
3.1.5	<i>AZO Electrodes</i>	22
3.2	NANOPARTICLES SYNTHESIS AND CHARACTERIZATION	22
3.3	BIOSENSOR CONSTRUCTION	24
3.3.1	<i>ITO Coated Glass Electrodes Characterization</i>	24
3.3.2	<i>Polymerization Conditions</i>	25
3.3.3	<i>Characterization of Sensor Assembly</i>	28
3.4	PERFORMANCE OF MIP SENSOR	30
3.4.1	<i>Calibration Curves</i>	30
4	 CONCLUSION	34
	REFERENCES	36
	APPENDIX A	41

Digital Fabrication of Transparent Electrodes for Simultaneously Optical and
Electrochemical Biosensor Applications

List of Figures

FIGURE 1: INDUCED CHANGES IN THE OPTICAL RESPONSE OF PHOTONIC CRYSTALS, SUCH AS STRUCTURED COLLOIDAL SILICA NANOPARTICLES, UPON MOLECULAR SENSING.	3
FIGURE 2: THREE-ELECTRODE SYSTEM ADAPTED DESIGN WITH INCREASED COUNTER ELECTRODE AREA.	4
FIGURE 3: RANGLES EQUIVALENT CIRCUIT WITH MIXED KINETIC AND CHARGE-TRANSFER CONTROL.	5
FIGURE 4: HOME-MADE RF MAGNETRON SPUTTERING SYSTEM: (A) VACUUM CHAMBER EXTERIOR; (B) VACUUM CHAMBER INTERIOR WITH 3 DIFFERENT MAGNETRONS.	7
FIGURE 5: AMINO-FUNCTIONALIZED SILICA NANOPARTICLES SYNTHESIS SETUP.	10
FIGURE 6: SCHEMATIC DIAGRAM OF THE SYNTHESIS OF AMINO-FUNCTIONALIZED SiO ₂ NPs WITH APTES AND TEOS.	11
FIGURE 7: ELECTRICAL RESISTIVITY, HALL MOBILITY AND CARRIER CONCENTRATION OF AZO THIN FILMS DEPOSITED FOR 1H, AT 2 MTORR AND AT ROOM TEMPERATURE AS A FUNCTION OF RF POWER.	14
FIGURE 8: OPTICAL TRANSMITTANCE OF AZO THIN FILMS DEPOSITED FOR 1H, AT 2.0 MTORR, WITH DIFFERENT RF.....	15
FIGURE 9: (A) XRD PATTERNS OF AZO THIN FILMS DEPOSITED FOR 1H AT 100 W, 2.0 MTORR AND THERMALLY TREATED AT DIFFERENT TEMPERATURES. THE HEATING RAMP WAS FIXED AT 5 °C/s. (B) OPTICAL TRANSMITTANCE OF SAME SAMPLES.....	15
FIGURE 10: EFFECTS OF POST-ANNEALING TEMPERATURE ON THE ELECTRICAL PROPERTIES OF AZO THIN FILMS DEPOSITED AT 100W, FOR 1H.	17
FIGURE 11: EFFECTS OF RTA HEATING RAMPS ON AZO THIN FILMS DEPOSITED FOR 1H AT 100 W, 2.0 MTORR AND THERMALLY TREATED AT 500 °C. (A) XRD PATTERNS OF THREE DIFFERENT HEATING RAMPS (B) OPTICAL TRANSMITTANCE OF RELEVANT RTA HEATING RAMPS.	17
FIGURE 12: PHOTOGRAPH OF THE FIRST LASER TEST IN ITO GLASS. EACH COLUMN IS ASSOCIATED WITH A FIXED SPEED (DECREASING FROM LEFT TO RIGHT), WHILE EACH ROW CORRESPONDS TO A FIXED POWER (DECREASING DOWNWARDS).	18
FIGURE 13: OPTICAL TRANSMITTANCE OF ITO THIN FILMS DEPOSITED ON GLASS AND PET SUBSTRATES.....	20
FIGURE 14: EDS ANALYSIS OF AN ITO ELECTRODE. (A) SEM IMAGE OF THE REGION IN WHICH THE EDS WAS CARRIED OUT. (B) EDS MAPPING OF BOTH ELEMENTS. (C) EDS MAPPING OF INDIUM. (D) EDS MAPPING OF TIN.	21
FIGURE 15: OPTICAL REFLECTANCE OF UNMODIFIED ITO COATED GLASS ELECTRODES.	22
FIGURE 16: SEM IMAGES OF POWDERED SiO ₂ -NH ₂ NPs: (A) 2000X ZOOM, (B) 25 000X ZOOM AND (C) 100 000X ZOOM.	23
FIGURE 17: FTIR SPECTRA OF SILICA NPs WITH AND WITHOUT AMINO FUNCTIONALIZATION. THE INSET GRAPH CORRESPONDS TO A MAGNIFICATION OF THE SPECTRA BETWEEN 4000 CM ⁻¹ AND 1500 CM ⁻¹	24
FIGURE 18: ELECTROCHEMICAL ANALYSIS OF UNMODIFIED ITO COATED GLASS ELECTRODES: (A) CV AND (B) EIS. THE CV ASSAY WAS PERFORMED FROM -0.7 V TO 0.7 V (3 SCANS), WITH A SCAN RATE OF 50 MV/S AND EIS WAS DONE WITH AN AMPLITUDE OF 0.01 V, WITH A LOGARITHMIC STEP TYPE AND A FREQUENCY RANGE OF 0.1 Hz TO 0.1 MHz.....	25
FIGURE 19: STUDY OF THE PY'S OXIDATION POTENTIAL. ONE CV SCAN WAS PERFORMED AT 50 MV/s, FROM	25
FIGURE 20: COMPARISON OF EIS SPECTRA OF THE RESULTING ELECTROPOLYMERIZATION OF DIFFERENT PY CONCENTRATIONS.	26
FIGURE 21: COMPARISON OF EIS SPECTRA OF THE RESULTING ELECTROPOLYMERIZATION OF PY 50 MM WITH DIFFERENT CV CYCLES.	27

Digital Fabrication of Transparent Electrodes for Simultaneously Optical and Electrochemical Biosensor Applications

FIGURE 22: SEM IMAGES AT 25000X ZOOM OF (A) $\text{SiO}_2\text{-NH}_2$ NPS DEPOSITED ON AN ITO ELECTRODE, (B) PPy FILM ELECTROPOLYMERIZED BY 5 CV CYCLES ON A $\text{SiO}_2\text{-NH}_2$ NPS/ ITO ELECTRODE.	28
FIGURE 25: SCHEMATIC REPRESENTATION OF THE STAGES PERFORMED IN THE FABRICATION OF MIP DEVICES.	30
FIGURE 26: EIS SPECTRA OF THE BIOSENSOR CALIBRATION PROCEDURE FOR MIP (A) AND NIP (B) DEVICES.	31
FIGURE 27: OPTICAL RESPONSES OF MIP (A) AND NIP (B) BIOSENSORS TO DIFFERENT CEA CONCENTRATIONS.	32
FIGURE 28: CALIBRATION CURVES OF MIP AND NIP BASED BIOSENSORS OBTAINED BY EIS MEASUREMENTS WITH INCREASING CEA CONCENTRATION.	32
FIGURE 29: CALIBRATION CURVES OF MIP AND NIP DEVICES OBTAINED BY REFLECTANCE ANALYSIS IN FUNCTION OF CEA CONCENTRATION.	33

List of Tables

TABLE 1: RESULTS OF THE OPTIMIZATION OF LASER PARAMETERS IN TERMS OF POWER AND SPEED. BLUE STANDS FOR CONDITIONS WITH NO VISIBLE EFFECTS; YELLOW MEANS THE PATTERNS WERE ONLY PARTIALLY ETCHED; GREEN IS FOR CONDITIONS WITH THE EXPECTED RESULTS; RED CORRESPONDS TO PARAMETERS, WHERE THE GLASS SUBSTRATE WAS ATTACKED AND FLAKED.	19
--	----

Motivation and Objectives

Cancerous diseases are one of the major concerns to public health and its early diagnosis is still the best tool to fight them. Monitoring specific biomolecules can show the existence or advance of a cancer disease, but this approach is still lacking a low-cost device that guarantees portability, high sensitivity and autonomy. Biosensor devices are the most promising approach to fulfill all these requirements, while also offering cheap production costs, sensitivity and reliable performance.

In the meanwhile, transparent electronics is the next generation of optoelectronics, with applications ranging from flat panel displays, to solar cells or medical devices. This technology is grounded on transparent conducting oxides like ITO due to their high optical transparency and low electrical resistivity. Since indium is a raw material on the European Commission critical list, substitute materials must be found.

The main goal of this dissertation was to develop transparent and flexible AZO electrodes using a low cost and fast fabrication method, which takes advantage of laser direct writing, to be used in biosensors for simultaneous electrochemical and optical detection. This thesis presents a new point-of-care concept for the detection, diagnostic and monitoring of cancer. The device combines the selectivity of plastic antibodies, used as sensing material, with the longer stability and lower costs of polymers, while offering a dual detection mechanism. The biosensor will be easy to use, transparent, cheap and applicable to the most frequent forms of cancer.

The novel combined approach proposed herein may lead to decreasing industry costs and presents sensing materials of high stability, when compared to the common natural antibodies used in immunosensing, increasing the sustainability for electronics. One of the core objectives is also to compare the properties of AZO with the ones of ITO and understand if it constitutes a conceivable replacement.

Digital Fabrication of Transparent Electrodes for Simultaneously Optical and
Electrochemical Biosensor Applications

1 | Introduction

Several theoretical notions, along with some of the techniques behind this work are presented throughout this chapter. Brief reviews of the state of the art on flexible electronics, transparent electronics and biosensors are also mentioned.

1.1 *Cancer Diagnosis*

Cancer is a major cause of death, averaging 262 deaths per 100 000 inhabitants in Europe, according to a study conducted by the World Health Organization. Among the most common forms of cancer are carcinomas of the colon, lung, liver, rectum, prostate and stomach [1, 2]. Some of these forms of cancer are curable or its effects can be retarded, however many will die from these conditions. Therefore, an early detection of cancer is fundamental and for this to be achievable, cancer diagnosis needs to be a faster, cheaper, easier and more precise process.

The first approach to cancer screening is still clinical examinations and exams such as biopsies and imaging. These techniques can be very informative, but they are usually effective only when the cancer is already developed. Moreover, a biopsy is an invasive and rather expensive procedure, which gives emphasis to the need for new diagnostic tools. Circulating tumor biomarkers can improve disease management because they are easily accessible and minimally invasive, and several biomarkers are already used to help clinical decision-making [3].

Biomarkers are molecules that act as indicators of biological processes. They are quantitatively measured and studied because they can be an alert for disease development at an early stage. Biomarkers can be found in the blood, urine, other body fluids or tissues and they facilitate the screening of diseases, help to control the progression, to follow response to treatment and to foresee a prognosis after clinical intervention [4].

When it comes to cancer, there are several types of biomarkers: proteins, nucleic acids, metabolites, exosomal biomarkers, circulating tumor cells, among others [5]. An ideal biomarker should allow the detection of a disease at early stages, offer high precision and sensitivity and be quickly quantifiable, reliable and inexpensive. Most biomarkers alone have limited sensitivity and specificity for clinical use, but recent advances in biomarker discovery owing to high-throughput techniques and nanotechnology-assisted approaches can improve current assays and help translate them into clinical practice [6].

One of the most widely used cancer biomarker is the carcinoembryonic antigen, which is a glycoprotein with high molecular weight (180-200 kDa) that can be found in the blood [7, 8]. CEA is involved in cell recognition and adhesion mechanisms, and therefore it is critical to the metastatic dissemination of carcinoma cells. CEA is produced by columnar and goblet cells in the gastrointestinal tissue throughout fetal development, therefore concentrations lower than 5 ng/mL are characteristic of healthy adults, since its production during adulthood should be insignificant [8]. Nonetheless, CEA alone is a nonspecific

Digital Fabrication of Transparent Electrodes for Simultaneously Optical and Electrochemical Biosensor Applications

tumor biomarker because high levels of this protein have also been associated with heavy smoking, hepatic disorders and numerous types of cancer [9].

CEA can be detected and quantified by standard clinical methods like enzyme-linked immunosorbent assay (ELISA), High Performance Liquid Chromatography (HPLC) or Gas Chromatography-Mass Spectrometry (GCMS), which are highly specific and sensitive [10]. However, they require specialized technicians, specific equipment, are too complex, time consuming and use expensive antibodies. In this context, biosensors are becoming an alternative to standard analytical methods, since they are cheap, fast, can be used in point-of-care and may incorporate artificial antibodies as recognition element.

1.2 Biosensors

A biosensor is an analytical device that translates the recognition of a specific biological analyte by a sensing element into a measurable signal by means of a transducer. Besides antibodies, the recognition can be made by biological tissue, DNA, microorganisms or enzymes. As for the transduction method, it depends on the kind of chemical or physical alteration that results from the sensing event, so a transducer may be optical, electrochemical, piezoelectric, magnetic, or thermal [10, 11].

1.2.1 Optical Biosensors

Optical biosensors detect analytes through the interaction of the optical field with a bio-recognition element. Its basic principle is to create an optical signal, colorimetric, fluorescent or luminescent, that is proportional to the concentration of the measured element [13]. There are two large categories of optical sensors: label-assisted sensing (using a tag or probe) and label-free that generates a signal directly upon binding of the target molecule [14]. One of the major advantages of label-free detection concerns the ability to detect biomolecules in their native state in real-time. Optical label-free biosensors are based on resonators, refractometers, surface plasmon resonance, photonic crystals (PCs), among others [15]. This works uses photonic crystals and consequently the emphasis is given to this sort of optical devices.

PC-based biosensors are able to strive with the competing technologies, since they offer a short assay time and a low-cost fabrication method, such as colloidal self-assembly or incorporation into hydrogels. Top-down approaches, like electronic beam lithography, nanoimprint lithography and electrochemical etching can also be used [15, 16]. PCs show distinct light manipulating properties, which are ideal for sensing applications, when defects and cavities are added to the material. This is explained by the fact that, opposing to most materials, PCs colors are correlated with their micro and nanostructure.

PCs are composed by alternating regions of spatially arranged dielectric materials with different refractive indices, which offer them high reflection efficiency at precise wavelengths. They show bandgaps or stop-bands, zones where the propagation of photons with specific energies is prevented due to the destructive interference of incident light with

Digital Fabrication of Transparent Electrodes for Simultaneously Optical and Electrochemical Biosensor Applications

reflections at dielectric boundaries [18]. Bragg reflectors are the simplest structure a PC can have, since it is just one dimension of a layered material with different refractive indices. When a three-dimensional matrix structure exists (3D-PCs) it is able to entirely prevent light propagation along a specific direction or within an exact wavelength range [19]. 3D-PCs are generally structured in opals, which are periodic 3D structures made by the crystallization of a colloidal dispersion of microspheres of silica and numerous polymers. Opals were ones of the first observed photonic crystals, have 24%-26% of air in their volume and when these voids are filled with a high refractive index material, the opal itself serves as a template that is later removed by wet chemical etching or calcination, leaving a new structure termed inverse opal [16, 19]. These new structures show an increased contrast in refractive index, higher efficiencies, larger surface area, macroporosity and enable a very accurate control over thickness and morphology of the deposited films [12, 20].

PCs have been interestingly applied to optical biosensors. The recognition of the target molecules induces changes, such as the crystal lattice or the refractive index, thus affecting the optical properties of the photonic structures. The responsiveness of the PC material is evaluated in terms of shifts in the wavelength of the peak reflectance and/or intensity variations (Figure 1). Therefore, the materials and structures of PCs allow tuning the diffracted wavelength, such as synthesis of colloidal nanoparticles with a certain size to obtain reflectance peaks at chosen wavelengths within visible light. Moreover, PCs can be integrated with electroactive polymers widening the range of applications of label-free sensing [19, 22].

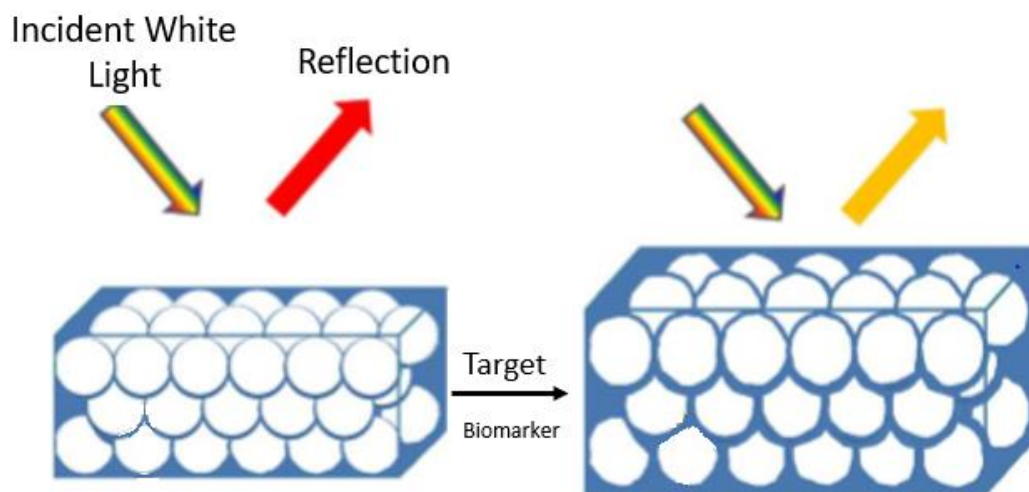


Figure 1: Induced changes in the optical response of photonic crystals, such as structured colloidal silica nanoparticles, upon molecular sensing.

1.2.2 Electrochemical Biosensors

Electrochemical sensors working principle consists in a flow of electrons between an electroactive species and an electrode surface. The sensing element on the transducer surface reacts with the analyte to produce an electrical signal that is proportional to the

Digital Fabrication of Transparent Electrodes for Simultaneously Optical and Electrochemical Biosensor Applications

analyte concentration. The electrode surface is usually a three-electrode system (Figure 2) comprised by a working electrode (WE), a counter electrode (CE) and a reference electrode (RE). To study the behavior of the analyte at the electrode/electrolyte interface both potential and current must be monitored. To do this, the system must be disturbed out of its equilibrium, which is done by applying potential and polarizing the WE anodically or cathodically and, to apply the potential, a standard constant potential is needed, hence the RE. The CE main purpose is to complete the current circuit, since the RE cannot be used as the current carrying electrode, as its potential would change. The opposite reaction from the WE occurs in the CE, therefore whenever the WE is being reduced, the CE is being oxidized [23].

Electrochemical sensors are categorized into three groups, according to the type of signal used for biosensing applications: amperometric, impedimetric and potentiometric [22, 23].

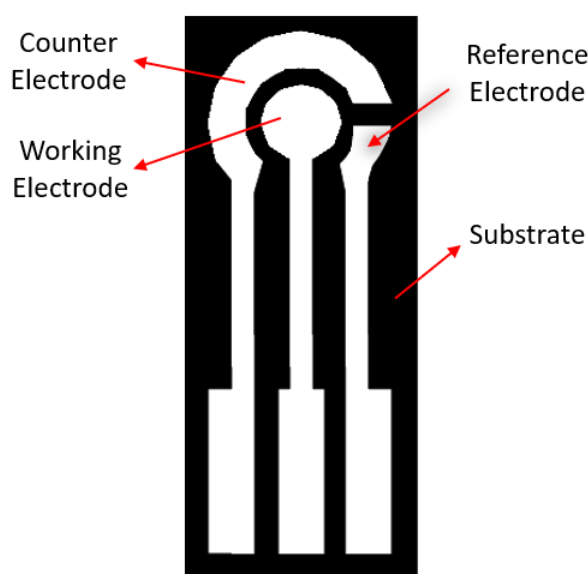


Figure 2: Three-electrode system adapted design with increased counter electrode area.

Amperometric sensors measure the current intensity between two electrodes due to a reduction or oxidation of an electroactive species. The analyte in study will change its oxidation state in the WE and the electron flux is then observed and proportional to the quantity of species electrochemically transformed [26]. The transducer emits a signal in the form of current, since it is the current change that indicates the presence of the analyte. Glucose sensor is the most well-known example of an amperometric biosensor [27]. Among amperometric techniques, cyclic voltammetry is widely used, in which the applied potential is swept between two values (forward and reverse between a minimum and a maximum) at a steady scan-rate [26]. In the voltammogram it is possible to analyze the obtained current at the electrode surface as a function of the applied potential. Thus, it is a very useful method for the electrochemical synthesis of polymers. The electrooxidation of the monomer and polymer film deposition can be precisely controlled through the number of scan cycles and scan-rate [28].

Digital Fabrication of Transparent Electrodes for Simultaneously Optical and Electrochemical Biosensor Applications

Impedimetric sensors measure the impedance of the system after immobilization of bi-layers at the electrode surface. This happens when molecules present at the interface between the electrode and the electrolyte have a strong impact on the overall impedance. When there is a change in charge-transfer resistance (R_{CT}) between solid and liquid interface, in the case of redox-active probes present in the electrolyte, the expected changes in the R_{CT} caused by molecular recognition or binding can then be measured [29]. This kind of biosensors are generally analyzed by electrochemical impedance spectroscopy, a technique that applies a range of AC frequencies and measures the impedance, i.e., resistive and capacitive properties [30]. EIS not only allows to know more about formation of double layer capacitance (C_{dl}), solution resistance (R_S), charge transfer resistance and diffusion transport, but also its results can be modeled by fitting with electrical equivalent circuit, such as the Randles circuit presented in Figure 3. [12]

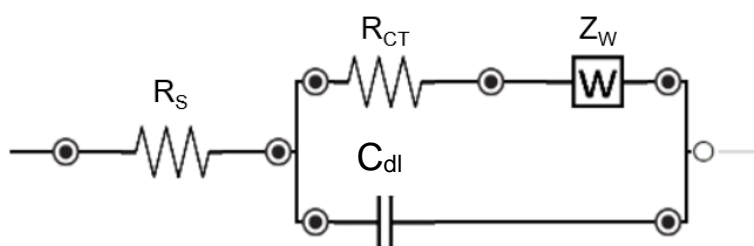


Figure 3: Randles equivalent circuit with mixed kinetic and charge-transfer control.

1.3 Molecularly Imprinted Polymers

The synthetic solution to mimic natural antibodies relies on using inexpensive plastic materials, which enable to maintain the required selective recognition and at the same time show longer stability. Plastic antibodies are produced by molecular imprinting, a process where the template interacts with functional monomers to form high affinity recognition sites on the polymer matrix, mimicking the binding sites of natural antibodies [31]. The template has a stable polymer grown around it. After polymerization and removal of the template, the recognition sites are exposed and exhibit high affinity for the specific target due to complementary size, shape and chemical functionality retained in the polymer matrix. In analogy, it is a comparable procedure to the creation of a plaster cast of a hand, only on a nanoscale [30, 31].

The molecular imprinting technique must be customized considering the properties of the target analyte and the type of sensor. Some common imprinting techniques are polymerization with thermal or photochemical initiation, either in bulk or surface imprinting, and electropolymerization.

Considering that the molecularly imprinted polymer shall be integrated in an electrochemical device, the chosen method is electropolymerization, since it allows the adjustment of several parameters that control the rate of polymer growth, thus enabling to control film thickness and morphology [28]. It also avoids the necessity for initiators. In

Digital Fabrication of Transparent Electrodes for Simultaneously Optical and Electrochemical Biosensor Applications

electropolymerization, the template is mixed with the monomer in a proper solvent and the polymeric matrix is created directly on the transducer surface by applying the required electrical conditions, making biomolecule immobilization and MIP synthesis a one-step process [34].

To create the imprinted surface binding sites, the selected monomer is of utmost importance, since it is essential for the success of the plastic antibodies. For detecting complex macromolecules like proteins, the presence of charged functional groups in monomers, in the pre-treated substrate prior to polymerization or on the surface of nanoparticles used in sensor design may improve protein binding [35].

Polypyrrole emerges as an excellent option to be used as the polymer in MIPs, because its deposition conditions are already well studied, as described in the literature [30, 34]. Moreover, the electropolymerization of Py may be precisely controlled, enabling to tailor the polymer film embedding the PC. The fine tuning of producing such MIP-based photonic sensor retains the versatility of PCs while broadening the responsiveness of the sensor due to electrochemical modulation.

In the present work, Py is electropolymerized on ITO substrates containing an opal structure of aminated silica NPs that shall be embedded on the polymer matrix. To construct the MIP, the template protein interacts with the charged surface of the NPs prior to Py electropolymerization. The absence/presence of the protein in the matrix changes the nanostructured layers of NPs within PPy. Therefore, protein detection based on this MIP may be evaluated both through electrochemical measurements and reflected analysis.

1.4 Transparent and Flexible Electronics

In the last years, a great interest emerged around room temperature processing of any devices that could be used for electronics, with special focus on flexible optoelectronics. Numerous papers were written about polymeric solutions and even paper to be used as substrates and the transparent conductive oxide (TCO) industry is booming. This area has been dominated by Indium Tin Oxide due to its outstanding optical and electrical properties [37]. However, suitable alternatives are being investigated nowadays, owing to the increased price of indium, the need for high processing temperatures and drawbacks in flexible applications [38]. AZO is a potential candidate by being an abundant, non-toxic and low-cost material with high chemical stability. Among all doped ZnO films, AZO demonstrates the lowest resistivity and it has been proved that it upholds its good properties when deposited at room-temperature, if RF sputtering conditions are optimized [37–39] This makes AZO suitable for flexible electronic applications.

Several applications have already been tested in polyethylene naphthalate (PEN) and polyethylene terephthalate (PET), such as foldable solar cells, plastic liquid crystals, heat reflecting mirrors among other with light weight, small volume and mechanical flexibility requirements. These polymers are some of the finest flexible substrates, since they offer excellent dielectric properties, thermal and chemical resistance, mechanical strength, low water absorption and good dimensional stability [42].

2 | Materials and Methods

This chapter reports the experimental techniques and methods used throughout this work. The first part reviews the fabrication of thin films. Secondly, the patterning of the electrodes by laser direct writing is fully explained and, lastly, the electrochemical procedures and assembly of the biosensor are described.

All chemicals employed in this thesis were of analytical grade. Aqueous solutions and washing were made with ultrapure milli-Q water.

2.1 AZO Thin Film Deposition

2.1.1 Physical Vapor Deposition – RF Sputtering

RF magnetron sputtering was used to deposit AZO thin films of about 200 nm on Corning 1737 glass and PEN at room temperature, resorting to a ceramic oxide target of ZnO:Al₂O₃ (98:2 mass ratio, 99.99% purity, ϕ : 2 inches). All substrates were 10 cm \times 10 cm and ultrasonically cleaned before being loaded into the chamber for 10 min with acetone, isopropyl alcohol and deionized water. The RF sputtering system used for the deposition of AZO was a home-made system developed at CENIMAT¹³/CEMOP, which does not have a load-lock for sample loading and removal (Figure 4). A pre-sputtering of 10 min was done to safeguard the reproducibility of the deposited thin films, since each deposition required taking the vacuum chamber to atmospheric pressure, where the target's surface could be contaminated.

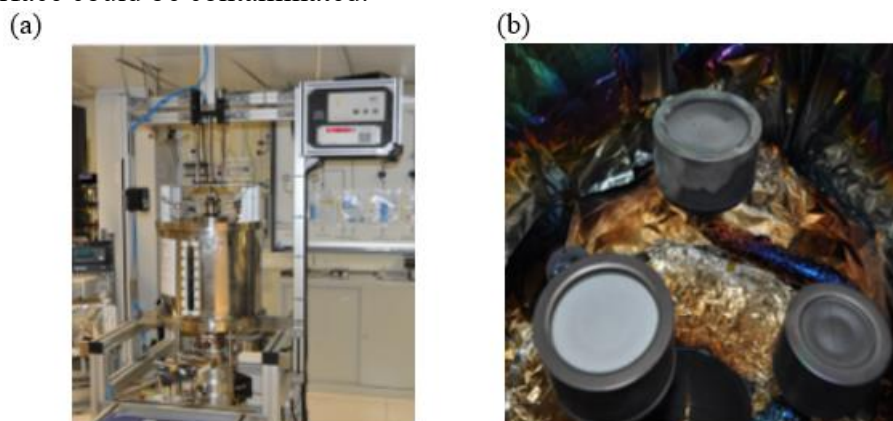


Figure 4: Home-made RF magnetron sputtering system: (a) vacuum chamber exterior; (b) vacuum chamber interior with 3 different magnetrons.

The processing parameters of the sputtering technique were optimized for both substrates, considering different conditions of RF power, percentage of oxygen in the Ar+O₂ mixture, deposition pressure and time. For glass substrates optimal depositions were obtained with 100 W RF power, 0% oxygen in the Ar+O₂ mixture and 2.0 mTorr of pressure. As for PEN, the best parameters were 100 W RF power, 2.0 mTorr of pressure but 1×10^{-5} mbar of oxygen. Both conditions were carried out at room temperature, for 1 hour, with 15 cm of target-to-substrate distance.

Digital Fabrication of Transparent Electrodes for Simultaneously Optical and Electrochemical Biosensor Applications

2.1.2 Rapid Thermal Annealing

Thin films produced by sputtering needed their dopants activated, therefore they were exposed to a fast heating from ambient temperature to 500 °C, with a heating ramp of 5 °C/s. As soon as the maximum temperature was reached, it was held for 1 min and then lastly quenched. The used equipment was an AS-One RTP system from Annealsys.

2.2 Laser Direct Writing

2.2.1 Apparatus

To pattern the chosen design of the three-electrodes configuration onto the substrates, a pulsed CO₂ infrared laser cutting system (Universal Laser System VLS 3.5) was used, with a focal length of 50.8 mm, wavelength of 10.6 μm and 2.0" lens (focus point of 0.127 mm). The laser setup comprises a laser source, a beam delivery system and the moving stages. The latter is the only controllable subsystem, a computer interface uses an RGB colour map that encodes specific laser power, speed and repetition rate, plus, the 2.0" lens can be swapped for a HPDFO (High-Power Density-Focusing Optics) lens, which offers a focus point of 0.025 mm.

2.2.2 Thin Film Etching

To pattern the chosen design of the three electrodes onto the substrates, Adobe Illustrator CC 2017 was used to design the pattern as a vector image input and, since the laser system works as a printer, the chosen RGB colours are converted into specific parameters. For the metal oxides in glass substrates the laser was operated at 35 W, 1000 pulses per inch and 1.27 m/s. As for the flexible substrates the conditions were the same, except for power, which was 10 W.

2.3 Thin Films Characterization

The characterization of thin films produced was an essential part of this work to assess their properties and quality, allowing the optimization of their production techniques. Hence, the metal oxides fabricated in the first part of this thesis were electrically, optically and chemically characterized.

2.3.1 X-Ray Diffraction

X-Ray Diffraction (XRD) results were recorded using a commercial X'Pert Pro MRD from PANalytical with a monochromatic Cu K α ($\lambda=1.54\text{\AA}$) radiation source, an applied current of 55 mA and voltage of 60 kV, in a 2θ range from 10° to -90° using a continuous scanning mode.

XRD is a non-destructive crystallographic technique used to analyze the structure of materials and reveal chemical composition. It allows a fast study of unit cell dimensions and phase identification of crystalline materials, determination of unknown samples, purity and textural measurements, such as grain orientation. Phase identification is done by comparing the acquired data with referential databases.

Digital Fabrication of Transparent Electrodes for Simultaneously Optical and Electrochemical Biosensor Applications

2.3.2 UV-Visible-NIR Transmittance Spectroscopy

UV-Vis-NIR spectroscopy is a characterization technique used to assess the optical properties of materials. The basic idea behind it is to measure the absorbed, transmitted or reflected light of a sample that has been illuminated by an incident light of varying wavelengths. This spectroscopy is also useful to quantify electronic transitions, since it allows to analyze accurately at which wavelength the samples absorb light and the frequency of light is correlated to energy.

The used equipment was a Shimadzu UV-3101PC UV-VIS-NIR Spectrophotometer, with a step of 2 nm, in a range between 250 nm and 2500 nm.

2.3.3 Scanning Electron Microscopy

For obtaining a morphological and chemical analysis of the fabricated materials, a SEM Zeiss Auriga CrossBeam Workstation was used. The thin films were coated with 15-25 nm of Au/Pd and the images were taken with a 5-15 kV of accelerating voltage and a mix of SE and BSE signals.

2.3.4 Four-Point-Probe Measurements

Samples of, usually, semiconductors can have their electrical impedance measured by a simple apparatus of a four-point probe. This device uses the outer pair of probes to apply a current in the sample, while the two inner probes measure its voltage. This way, the substrate resistivity can be obtained. By having this four-point probe, with separation of current and voltage by different electrodes, this method eliminates contact resistance from the measurement, making it a more accurate one.

2.3.5 Hall-Effect Measurements

The Hall effect is a complex notion that comes from an electric current flowing through a sample in a perpendicular direction to a magnetic field, which applies a transverse force on the moving electrons, pushing them to one side of the conductor. The charges will accumulate, producing a measurable voltage between the two sides of the sample, called the Hall Voltage. Hall effect measurement systems are sophisticated instruments capable of determining numerous material parameters, such as Hall voltage (V_H), Hall coefficient (R_H), resistivity (ρ), carrier mobility (μ) and carrier conductivity type. The used equipment was a HL5500PC from BioRad.

2.3.6 Contact Profilometry

Every deposition had a small piece of substrate covered with Kapton tape, so the thickness of the film could be measured. These measurements were done with profilometer Ambios XP-Plus 200 Stylus, with a stylus tracking force of 10 mg and minimum speed of around 0.01 mm/s.

2.4 Biosensor Assay

2.4.1 Apparatus

Electrochemical measurements were performed using a Metrohm Autolab potentiostat/galvanostat (PGSTAT320N), controlled by NOVA 2.1 software. The interface

Digital Fabrication of Transparent Electrodes for Simultaneously Optical and Electrochemical Biosensor Applications

between the electrodes and the potentiostat was acquired from DropSens (DRP-DSC4MM) but it only had sufficient height to read the PET/PEN electrodes. Therefore, for the glass substrate with three-electrodes configuration a homemade interface device was built at CENIMAT. The fabrication protocol and pictures of the interface can be consulted on Appendix A.

The optical properties of the biosensor during the several steps of fabrication and in response to target biomarker were analyzed in terms of reflectance and the spectra (190-1110 nm) were recorded on a Thermo Scientific UV-Vis spectrophotometer (Evolution 220).

2.4.2 Electrochemical Procedures

The electrochemical studies comprised cyclic voltammetry to electropolymerize the monomer pyrrole (Py) and electrochemical impedance spectroscopy (EIS) analysis to follow sensor construction and response. The CV scans were performed from -0.2 V to 1.0 V with a scan rate of 50 mV/s. EIS studies were made in open circuit potential using a sinusoidal potential perturbation with 0.01 V of amplitude and 50 frequency values, logarithmically distributed over a frequency range from 0.1 Hz to 0.1 MHz. The EIS assays were all achieved using 5.0×10^{-3} M of $[Fe(CN)_6]^{3-}$ and 5.0×10^{-3} M of $[Fe(CN)_6]^{4-}$ as redox probe, prepared in PBS buffer (10 mM, pH 7.4) The EIS data was fitted to a Randles equivalent circuit using 2.1 Nova Software from Autolab. Every assay was ran in triplicate to rule out errors or experimental bias.

2.5 Sensing Material Assembly

2.5.1 Silica Nanoparticles Synthesis and Functionalization

The imprinted material was assembled in several stages. The first one consisted on the sol-gel synthesis of monodispersed spherical silica (SiO_2) nanoparticles through an adaptation of the Stöber method [43][44][45], which comprises the base-catalyzed hydrolysis of tetraethyl orthosilicate (TEOS) and (3-aminopropyl)triethoxysilane (APTES) in ethanol.



Figure 5: Amino-functionalized silica nanoparticles synthesis setup.

Digital Fabrication of Transparent Electrodes for Simultaneously Optical and Electrochemical Biosensor Applications

Two separate solutions were prepared: solution A and B. Solution A was a mixture of ethanol in the same volume as the sum of APTES and TEOS: 1.565 mL of ethanol, 49 μ L of APTES and 1.516 mL of TEOS. Solution B consisted of 2.25 mL of water, 0.828 mL of ammonia and 18.792 mL of ethanol. As shown in Figure 5, solution B was placed in a three neck round bottom flask with a Graham condenser attached, while A was put in a flask and both were mixed, at 50°C, for 20 min. Then, solution A was slowly added to the round bottom flask, at 900 rpm. The reaction was done at 50°C for 2h, at 300 rpm and, in the end, the round bottom flask was placed on ice, to certify that the reaction had finished. The resulting aminated SiO₂ NPs are positively charged for increased affinity towards the highly glycosylated protein biomarker and a brief schematic of the reaction can be seen in Figure 6.

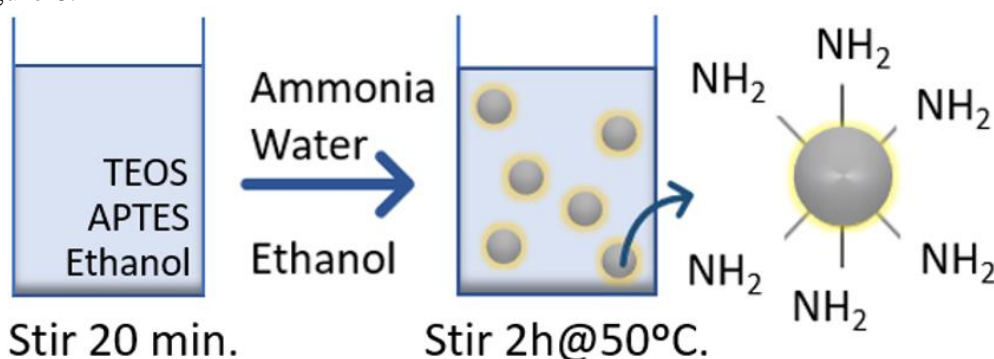


Figure 6: Schematic diagram of the synthesis of amino-functionalized SiO₂ NPs with APTES and TEOS.

2.5.2 Nanoparticles Deposition

The second stage was a vertical deposition of the colloidal SiO₂ NPs in order to obtain highly ordered assembled layer films. The entire chip was placed in a vial, where it stayed dipped in a solution containing 1 mg/mL of NPs, with an approximate angle of 65° for 3 days. Several vials were prepared in batches and stored in controlled conditions, at 50 °C. To guarantee uniformity across the deposition, the WE was cleaned beforehand with Ex-tran, MiliQ water, ethanol and acetone. To remove the surplus of deposited material, NaOH 3 M was used.

2.5.3 Molecularly Imprinted Photonic Sensor Construction

The next step was to create the plastic biomarker mold. To attain it, CEA (10 μ g/mL in PBS buffer 10 mM, pH 7.4) was incubated within the assembled colloidal NPs for 30 min, followed by a washing step and the electropolymerization of Py (50 \times 10⁻³ M in PBS buffer 10 mM, pH 7.4) by applying 5 CV cycles from -0.2 V to 1.0 V, using a scan rate of 50 mV/s (the electropolymerization conditions have been previously optimized as described ahead in section 3.3.2). After PPy formation embedding the NPs and CEA biomarker, the template CEA was removed by incubation with oxalic acid 0.5 M for 2 hours and the final imprinted photonic polymer was equilibrated in PBS buffer (10 mM, pH 7.4) for 30 min before subsequent analysis. This procedure shaped a molecularly imprinted opal photonic structure with high affinity to CEA, which was named MIP.

A non-imprinted material (NIP) was assembled in parallel, following a similar protocol and identical solutions, excluding the incubation step with CEA solution that was

Digital Fabrication of Transparent Electrodes for Simultaneously Optical and Electrochemical Biosensor Applications

replaced by incubation with PBS buffer (10 mM, pH 7.4). All steps of MIP/NIP construction were followed optically through reflectance analysis and electrochemically using EIS, as described above.

2.6 Biosensor Characterization

2.6.1 Fourier-Transform Infrared Spectroscopy

A Nicolet iS10, from Thermo Scientific, was used for infrared spectroscopy assays for chemical characterization of samples. The data was collected using an Attenuated Total Reflectance (ATR) sampling accessory equipped with a single bounce germanium crystal. The spectra were acquired with 250 scans and a 4 cm^{-1} resolution, in the range of $4000\text{-}525\text{ cm}^{-1}$. This technique reveals the composition of materials and can be used for identification and confirmation of produced materials.

2.6.2 Scanning Electron Microscopy

SEM studies were performed on a FEI Quanta 400FEG ESE/ Edax Genesis X4M, from Thermo Fisher Scientific, operating at high and low vacuum at 15 kV and using a SE signal. Sample preparation involved the deposition of a 15 nm AuPd thin film to ensure good electrical conductivity at the surface. SEM images were used to analyze both the size and monodispersity of the colloidal SiO_2 NPs as well as the order of opal films assembled on ITO chips.

2.6.3 Analytical performance of the biosensor

The analytical performance was evaluated through the rebinding properties of the imprinted films. Calibration curves were obtained by incubating the WE with increasing concentrations of CEA (1 ng/mL to 10 ng/mL) prepared in PBS buffer (10 mM, pH 7.4). The calibration curves were analyzed electrochemically by EIS measurements and the graphs are depicted as R_{CT} against the logarithm of CEA concentration. Simultaneously, the ability to recognize increasing amounts of CEA was evaluated optically, based on the alterations induced in the reflectance spectra of the opal photonic structure and plotting the calibration slope. Both methods are used to assess the overall biosensor performance in terms of linear range and limit of detection. The sensor prepared with the NIP was also evaluated as the negative control.

3 | Results and Discussion

Along this chapter, all relevant results obtained throughout this work are presented, discussed and compared to previously published papers.

The first section, 3.1., refers to the optimization and fabrication of transparent electrodes. In the following sections, the production of a viable sensing device using ITO as proof of concept is described. Thus, section 3.2 displays the results related to the synthesis and characterization of silica nanoparticles prior to assembly of the photonic crystal. In section 3.3 all the results regarding the sensor construction are shown and, finally, section 3.4 presents the results obtained from sensor response studies.

3.1 Optimization, Production and Characterization of TCO's

3.1.1 AZO Deposition Optimization

The first objective of this work was to fabricate AZO thin films with thicknesses between 100 nm and 200 nm on glass and flexible substrates that showed low electrical resistivity and high optical transmittance, simultaneously.

RF magnetron sputtering is a great technique for the deposition of transparent oxides, as it offers a large coverage, good adhesion, high film density and, most importantly, compatibility with low or even room temperatures. Nonetheless, sputtering parameters have a strong impact on thin films quality, significantly affecting the growth and crystal structure of the produced films. To optimize the fabrication process, different RF power and post-thermal treatment were tested. The target-substrate distance was kept at 15 cm for all depositions. An AZO target from Alineason Materials with 2% of Al was used to deposit all AZO thin films.

3.1.1.1 RF Power

One of the main controllable parameters on RF magnetron sputtering is the RF power, which is responsible for transferring kinetic energy to the bombarding ions that hit the target material. Higher RF powers lead to more ejected species and, in result, higher deposition rates that create thicker thin films.

Four different RF powers were tested (75 W, 100 W, 125 W and 150 W), as shown in Figure 7, which presents the electrical characterization of the produced AZO samples.

Each sample was measured with the profilometer and the thickness of the films increased linearly with the RF power, from 172 nm to 201 nm. From the plot in Figure 7, it can be concluded that higher RF powers and, consequently, thicker films lead to higher electrical conductivity and carrier mobility and concentration. However, at 150 W this behavior changes, suggesting that some other mechanisms are acting up. Increasing RF power promotes particles collision and higher crystallinity in the obtained films, which have bigger grain size and less oxygen vacancies, resulting in higher resistivities and possible superficial defects.

Digital Fabrication of Transparent Electrodes for Simultaneously Optical and Electrochemical Biosensor Applications

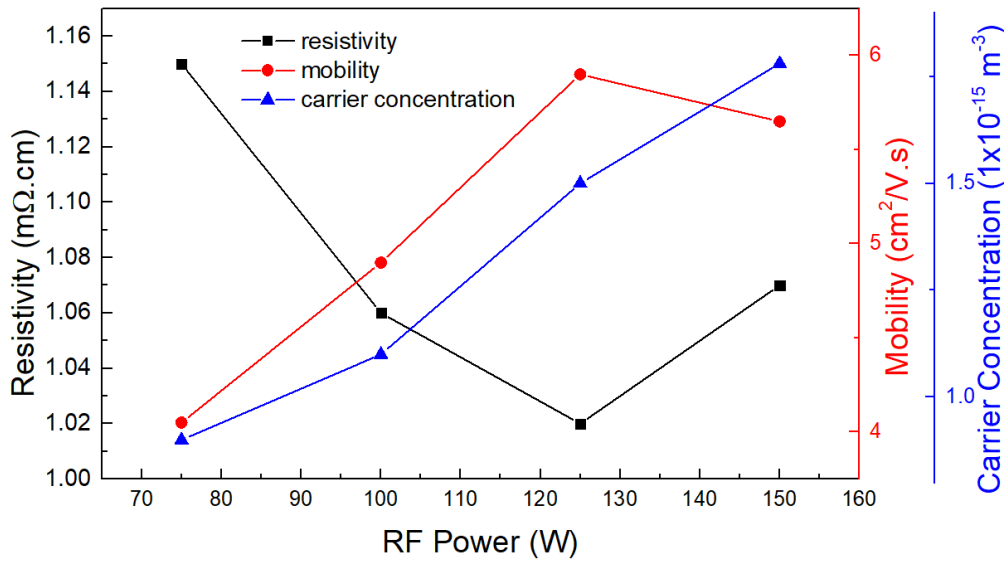


Figure 7: Electrical resistivity, Hall mobility and carrier concentration of AZO thin films deposited for 1h, at 2 mTorr and at room temperature as a function of RF power.

The increment in RF power induces the ejected species to reach the substrate with a higher energy, allowing them to move along its surface and form little clusters. This mechanism is often observed in polycrystalline oxides, where the rise in power density favors grain growth due to the increased mobility of the ejected species. These species migrate to new positions in the crystalline lattice where its connections are optimized, supporting nucleation and grain growth and, consequently, higher crystallinity in the films. The increased carrier concentration is associated with less oxygen being weakly linked to the film surface and the lack of O₂ in the sputtering atmosphere not being able to compensate the vacancies.

Figure 8 illustrates the optical characterization of thin films deposited with different RF powers. From the optical spectra, it is visible that the 75 W sample is not very crystalline, but all the other depositions led to highly transparent thin films in the visible range, being the lowest value of transmittance 76% in this range. In the visible spectrum, the transmittance decreases with the increase of RF power, but the opposite behavior is depicted in the NIR region. The highest transmittance in the visible region is from the 100W sample, although it is the lowest for higher wavelengths, which means this sample has high free carrier concentrations, since they are responsible for the photon absorption in this region [46]. Increased RF power led to higher transmittances in the NIR region, which can be related to lower bandgaps that are associated with high crystallization of the thin films. Therefore, it can be concluded that increasing the RF power of the depositions leads to a higher level of crystallization of the AZO thin films [46, 47].

Considering the results from the highest power applied, 150 W, it is concluded that it did not present the best transmittance in the visible region and high powers often break the ceramic targets. The condition of 100 W was chosen as the most balanced, due to its behavior in the NIR region and considering that it offers the highest average transmittance

Digital Fabrication of Transparent Electrodes for Simultaneously Optical and Electrochemical Biosensor Applications

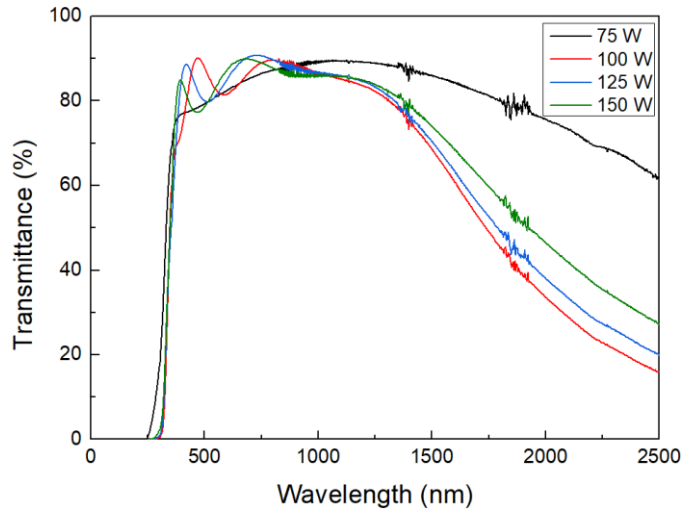


Figure 8: Optical transmittance of AZO thin films deposited for 1h, at 2.0 mTorr, with different RF powers and no thermal treatment.

in the visible region. The electrical characterization is not the best, but bearing in mind all the variables, 100 W is a condition that guarantees good results. Increasing RF power enhances the trap probability of substitutional Al and interstitial Zn, that act as donors, leading to more efficient doping [47]. That is also justified by decreasing resistivity in function of RF power.

3.1.1.2 Rapid Thermal Annealing

To obtain the best possible conditions, a rapid thermal annealing was always performed on AZO thin films on corning glass substrates. This thermal treatment consisted in 1 minute of high temperatures that ranged from 200 °C to 600 °C, with the purpose of dopant activation. Flexible substrates, due to being polymeric, were not compatible with this

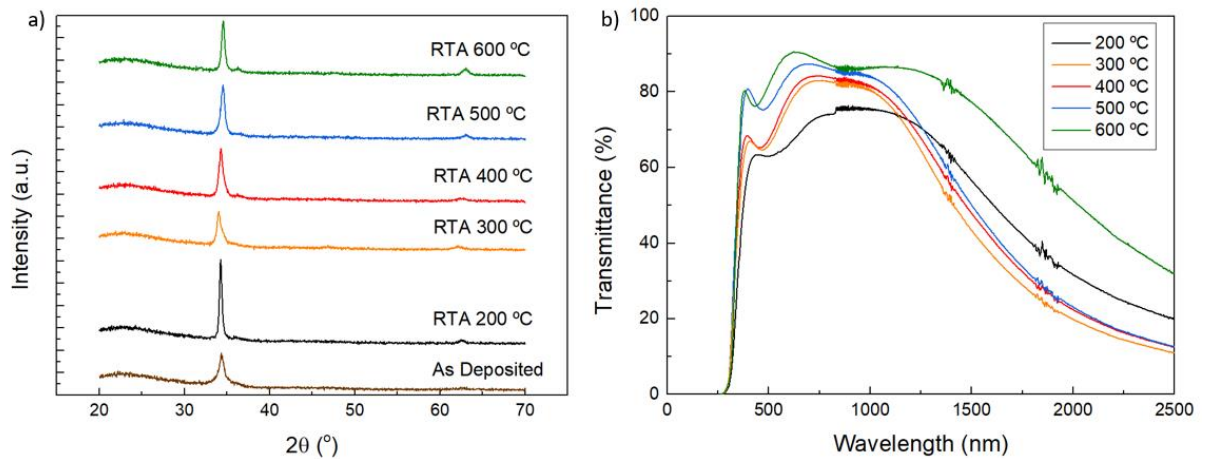


Figure 9: (a) XRD patterns of AZO thin films deposited for 1h at 100 W, 2.0 mTorr and thermally treated at different temperatures. The heating ramp was fixed at 5 °C/s. (b) Optical transmittance of same samples.

Digital Fabrication of Transparent Electrodes for Simultaneously Optical and Electrochemical Biosensor Applications

treatment, as the high temperatures surpassed their melting point. Figure 9a presents the XRD analysis of the different temperature conditions tested by rapid thermal annealing (RTA).

The XRD diffraction patterns of the several AZO thin films show a polycrystalline hexagonal wurtzite structure, with a preferential orientation along the c -axis (002), perpendicular to the substrate plane, since this plane formation requires low energy [46]. Broader peaks and smaller intensities represent smaller crystallite size in materials, suggesting that higher RTA temperatures led to further crystallization of the AZO thin films. Peak position shifts towards higher angles are related with the variations in interatomic distances, mainly due to increased dopant activation with the rise of RTA temperatures, since the thickness remained the same. The intense peak associated with the lowest RTA temperature shows an unexpected behavior that can be justified by a larger area being analyzed by the x-ray beam, due to human error in the sample characterization.

The optical transmittance of the films was also inspected and measured in a wavelength from 250 nm to 2500 nm, to include also the near infrared region, as shown in Figure 9b. Each condition shows a different average transmittance in the visible range, evidencing a proportional relation between transmittance and temperature, since the lowest RTA temperature is associated with the lowest transmittance value and for higher temperatures, the transmittance increases accordingly. From the previous XRD analysis, it was concluded that increased annealing temperatures led to higher crystallinity in films, therefore another conclusion can be made: the structural properties of the thin films influence their transparency in the visible region. As for the near infrared region (1500-2500 nm), the spectra seem to hint to a similar behavior, except for the 200 °C spectrum, which shows some incongruencies. The curve's profile depicts a strong role of the free carrier concentration, because the reduction of transmittance at longer wavelengths is a result of the absorption of photons by free carriers. Therefore, materials highly doped with free electrons present a much lower NIR optical transmittance [46].

Since an increase in carrier concentration leads to blockage of the lowest states in the conduction band and an increase in the optical bandgap, the analysis of this regions allows the conclusion that lower optical transmittances are associated with higher bandgaps, which in turn, are associated with a lower state of crystallization.

Figure 10 shows the electrical characterization of samples with different post-annealing temperatures. The decrease in resistivity with the increase in temperature was due to the fact that the annealing temperature can induce a structure rearrangement and influence growth of grain size, thus reducing grain boundary scattering. The increase of carrier concentration is attributed to the development of the oxygen vacancies and the increase of mobility is justified by an improvement in porosity and quality of AZO films, since the crystallite size becomes larger with a higher temperature annealing [48].

Digital Fabrication of Transparent Electrodes for Simultaneously Optical and Electrochemical Biosensor Applications

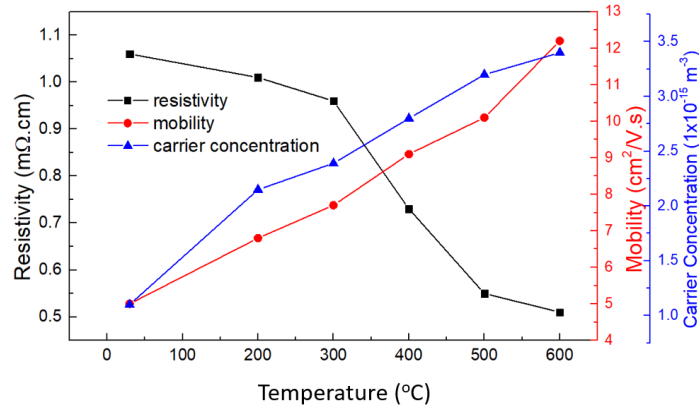


Figure 10: Effects of post-annealing temperature on the electrical properties of AZO thin films deposited at 100W, for 1h.

The heating rate of the post-thermal annealing was also optimized and Figure 11 presents the performed characterization. Figure 11a shows the XRD analysis of three different heating rates, where it is visible that the slower rate creates more crystalline thin films, due to its more intense peak and reduced full width at half maximum. The other rates express an analogous behavior, with the exception that the 150 °C/s ramp shows a new peak at $2\theta = 63.2^\circ$, associated with the (226) plane of the cubic structure of Al_2O_3 [48].

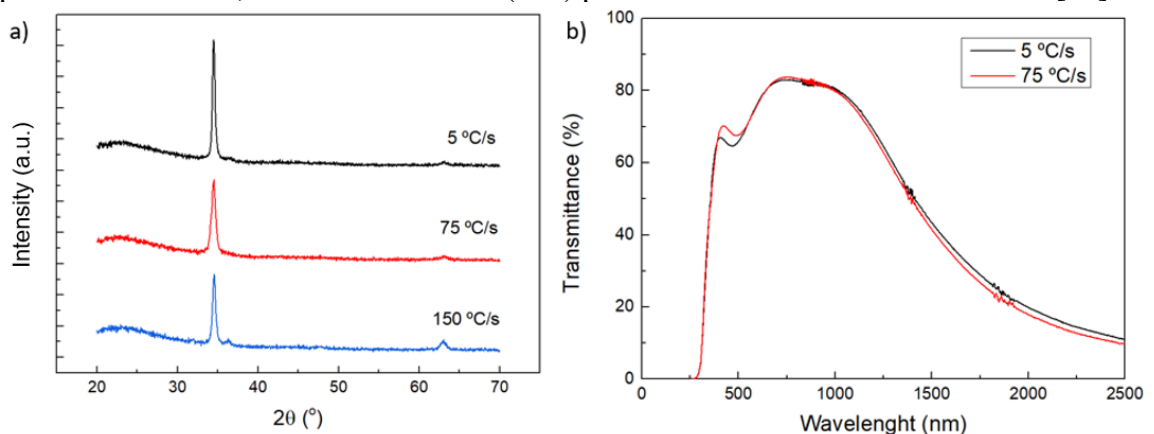


Figure 11: Effects of RTA heating ramps on AZO thin films deposited for 1h at 100 W, 2.0 mTorr and thermally treated at 500 °C. (a) XRD patterns of three different heating ramps (b) Optical transmittance of relevant RTA heating ramps.

Figure 11b illustrates the optical performance of the most relevant heating rates from XRD analysis. Slight differences are present in the visible region, where the 75 °C/s condition presents higher transmittance, but, overall, optically this parameter is insignificant.

The chosen RTA condition regarding the heating ramp was 5 °C/s, since optically all the tested conditions were identical, but the XRD data showed increased crystallinity when compared to the other samples. A maximum temperature of 500 °C was also the selected

Digital Fabrication of Transparent Electrodes for Simultaneously Optical and Electrochemical Biosensor Applications

parameter, because even though an annealing of 600 °C shows higher optical transmittance in the NIR region, which points towards a higher optical bandgap and crystallization of the thin films, the XRD and electrical characterization are similar to an annealing performed at 500 °C.

3.1.2 Laser Parameters – Glass Substrates

Having optimized the substrate materials, the next step was to study the effects of laser power and speed, with the objective of manufacturing electrodes with the best possible quality. To that end, a systematic study was conducted where the same ITO coated glass substrate was tested with multiple combinations of laser speeds and powers, as shown in Figure 12. The study started with ITO since it was commercial and therefore more reliable.

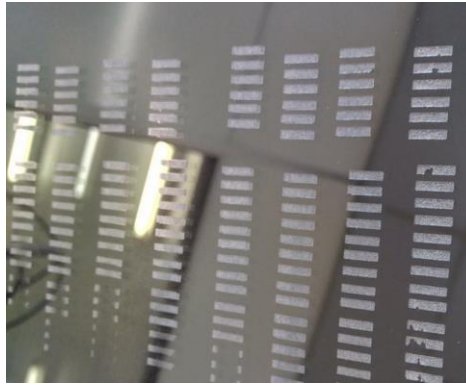


Figure 12: Photograph of the first laser test in ITO glass. Each column is associated with a fixed speed (decreasing from left to right), while each row corresponds to a fixed power (decreasing downwards).

The laser works as a printer, having a vectorial image input and moving along two axis, eroding material as it moves. In this case, the laser is used to etch the TCO thin films. A simple rectangle pattern was chosen to maximize the ITO glass substrate and the number of pulses per inch was kept at 1000, as it was not a relevant parameter for these engravings. The patterns were ablated as a matrix, where each column was associated with a scanning speed and the rows corresponded to a specific laser power. The laser power was studied between 10 W and 50 W, while the laser speed varied between 0.38 m/s and 1.27 m/s. The laser interface displayed laser power and speed in a percentual scale, where 100% corresponded to the maximum power and speed achieved by the device.

This study allowed to identify four distinct aftereffects of the laser direct writing: No visible etching, which happens with combinations of lowest powers and highest speeds; Partial pattern engraving, that occurs with relatively low scanning speeds and lowest powers; Good pattern engraving, that shows quality etching and results from medium to high laser powers combined with medium to low speeds; Substrate degradation, that happens when higher powers and lower speeds are applied. These conditions and effects are summed up in the color map of Table 1.

Digital Fabrication of Transparent Electrodes for Simultaneously Optical and Electrochemical Biosensor Applications

On the first case, the amount of energy that is transmitted to the ITO glass is not enough to break the chemical bonds for the occurrence of etching. When the speed decreases, the amount of energy transferred over time to the same substrate spot rises, especially in the

Table 1: Results of the optimization of laser parameters in terms of power and speed. Blue stands for conditions with no visible effects; Yellow means the patterns were only partially etched; Green is for conditions with the expected results; Red corresponds to parameters, where the glass substrate was attacked and flaked.

		SPEED (%)							
		100	90	80	70	60	50	40	30
POWER (%)	100	Green				Red			
	90	Green					Red		
	80	Green						Red	
	70	Green							Red
	60	Yellow				Green			
	50	Blue		Yellow					
	40	Blue			Yellow				
	30	Blue					Yellow		

pattern edges, where the laser changes position and ends up uncontrollably dispersing thermal energy. Therefore, partial patterns result from a fusion of dispersed thermal energy and increased laser power. Good pattern engraving happens when the combination of dispersed thermal energy and applied laser power over time are just enough to deteriorate the ITO thin film, without affecting the glass substrate. This results in a fully resistive pattern. The last event, when substrate degradation exists, is justified by very high amounts of energy being distributed over longer periods of time to the same spot, which are also combined with increased thermal dispersion, resulting not only in the breaking of chemical bonds in the ITO thin film, but also in the glass underneath, perforating, damaging it permanently and even leading to some layers to flake, as can be seen in the last column of Figure 12.

This optimization was done at the naked eye, so an electrical characterization was needed. Four-point probe technique was used to assess if the patterns that were fully etched and did not show glass disintegration were, in fact, fully resistive. All the conditions marked as red and green in Table 1 were unable to conduct any current, therefore could not be read by the four-point probe technique, while conditions marked as yellow could be read but showed high discrepancy. As for all the conditions checked as blue, since ITO is a good conductive oxide, their electrical behavior was outstanding and homogeneous, showing $20 \Omega/\text{square}$ of sheet resistance.

Electrical characterization confirms that when a pattern is fully etched, the conductive transparent oxide is carved to the point of cancelling any electrical current, acting like an open circuit. Some of the successful conditions were then tested with serial production of the actual three-electrode design and some disparities in the results were noticed. It was concluded that operating the laser system for long periods of time on the same ITO glass

Digital Fabrication of Transparent Electrodes for Simultaneously Optical and Electrochemical Biosensor Applications

substrate led to an increase of its temperature, resulting in thermal effects that were hard to predict.

By trial and error, the chosen laser conditions are 35 W of power and a scanning rate of 1.27 m/s. This laser speed is the system's maximum and it was chosen to prevent any further local thermal dispersion and even though several combinations worked, these parameters guarantee a perfect pattern etching at all times. It is important to mention the infrared laser leads to a higher absorption coefficient of ITO, helping the etching process, but also increasing the thermal effects. This could be reversed by using an UV laser as an alternative.

The same parameters were tested on the AZO glass substrates and the results were very similar, so the optimal laser conditions for this material remain the same.

3.1.3 Laser Parameters – Flexible Substrates

The laser parameters for etching PET substrates had already been optimized by another researcher in CENIMAT, therefore those conditions were the first to be tested on the ITO on PET electrodes. Power was set to 10W and speed was 1.27 m/s and these conditions worked perfectly, eroding the layer of oxide from the polymeric substrate. Since PET, while transparent in the visible range, shows a light yellowish tone, it makes the absorption of energy coming from the laser to be higher, making its surface more prone to etching. These facts are sustained by Figure 13, which shows the optical transmittance of ITO on both glass and PET.

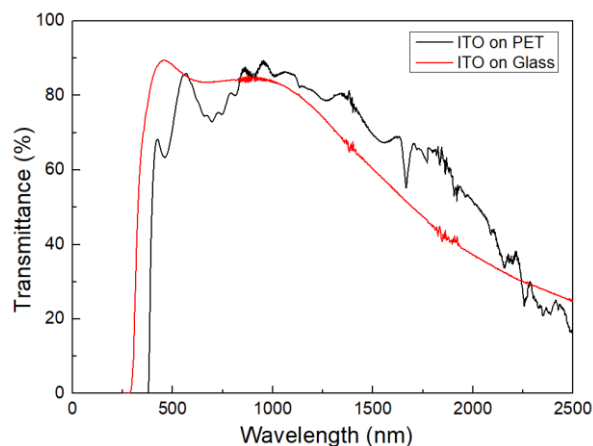


Figure 13: Optical transmittance of ITO thin films deposited on glass and PET substrates.

ITO electrodes deposited on PET substrates displayed a sheet resistance of 35 Ω /square and it remained the same after laser direct writing.

3.1.4 ITO Electrodes

Opposite to the AZO electrodes whose fabrication procedure was fully optimized, ITO substrates were acquired already deposited and the only optimization step was the electrode patterning, showed in the section above. After the laser direct writing, ITO electrodes were morphologically and chemically characterized by SEM and EDS. These analyses are shown in Figure 14.

Digital Fabrication of Transparent Electrodes for Simultaneously Optical and Electrochemical Biosensor Applications

Figure 14a shows a SEM image of a region on the ITO surface where a laser patterning has been done. The surface is smooth with some scratches, which are probably waste from the laser etching and the area where material has been removed is clearly visible.

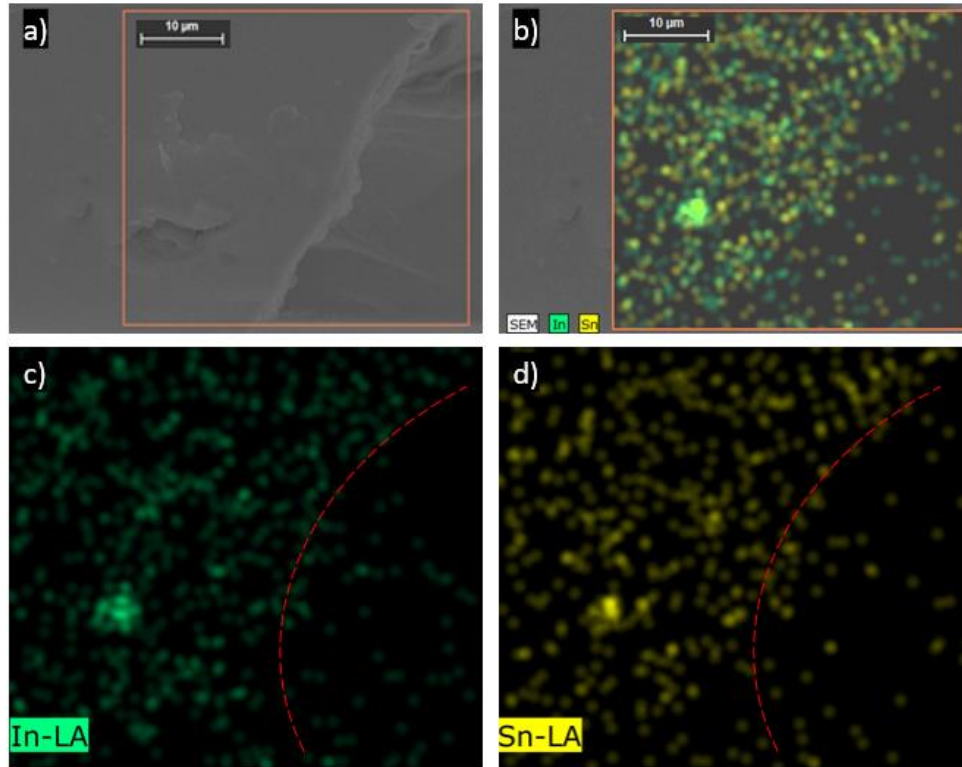


Figure 14: EDS analysis of an ITO electrode. (a) SEM image of the region in which the EDS was carried out. (b) EDS mapping of both elements. (c) EDS mapping of indium. (d) EDS mapping of tin.

Figure 14b is an EDS image of the combination of the analyzed elements and it proves that ITO has indeed been removed in that region, as a visible lack of indium and tin can be observed. Figure 14c,d reinforce this evidence, as they represent the distribution of each element and, again, the right section of the images are clearly poorer in indium and tin.

Since the objective was to obtain a silica photonic crystal film on the ITO electrodes, these were also characterized in terms of reflectance as a control. Figure 15 illustrates the reflectance of a clean electrode on the visible region.

The substrate is quite transparent and it is not expected to interfere in the subsequent measurements of reflectance of the photonic material. The refractive index of ITO decreases linearly with higher wavelengths, showing an average index of 1.95 ± 0.21 in the visible range [49].

Digital Fabrication of Transparent Electrodes for Simultaneously Optical and Electrochemical Biosensor Applications

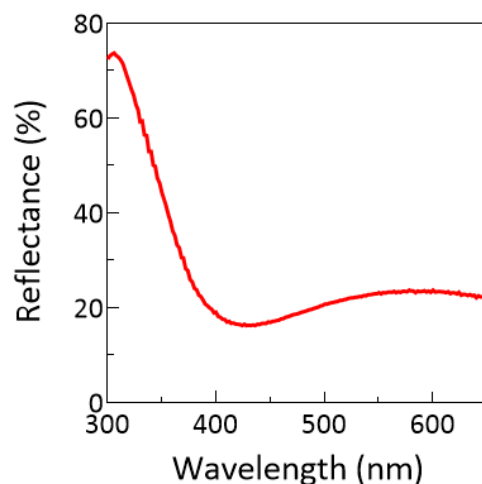


Figure 15: Optical reflectance of unmodified ITO coated glass electrodes.

3.1.5 AZO Electrodes

AZO substrates after being patterned by laser direct writing displayed the same electrical properties already shown above and their optical transmittance remained alike, although due to equipment limitations the measurements showed lower values. Primary electrochemical assays on AZO electrodes displayed a very inconsistent response, since AZO can be highly susceptible to humidity, therefore aqueous solutions did not react very well with these electrodes. Further studies would be needed to guarantee a reliable behavior from AZO to this biosensing application, so since ITO was a better, more reliable and the go-to material when it comes to transparent electronics, AZO was optimized but not used as proof-of-concept for the biosensing application of this dissertation.

3.2 Nanoparticles Synthesis and Characterization

The preparation of the biosensor embraces a bottom-up approach and the silica nanoparticles synthesis was the first step in the construction of the device. The nanoparticles must be organized in an ordered array to create a structural scaffold capable of being infiltrated by the CEA protein and the polymer, originating an opal film. Taking advantage of the high tunability of silica nanoparticles synthesized by Stöber method, APTES was included in the reaction mixture to obtain particles with amino functional groups. Briefly, in the Stöber method, metal alkoxides and water react in the presence of an acid or base to form a one phase solution that goes from solution to gel. Its properties depend highly on the catalyst. Ammonia was chosen in this work because bases form highly branched clusters due to rapid hydrolysis condensation of TEOS, instead of weakly crosslinked linear polymers [50]. Gelation then happens by linking of the clusters. Again, an alkaline medium favors the interlinking of silica clusters. Since complete hydrolysis is difficult to achieve, condensation occurs. In condensation, water or alcohol molecules are formed, along with oxygen bridges. These reactions are initiated at several sites and when enough bonds are made, they interact to form colloidal particles (sol) and in time they too link together to form a 3D network, which at gelation gets increased viscosity (gel) [42, 43].

Digital Fabrication of Transparent Electrodes for Simultaneously Optical and Electrochemical Biosensor Applications

The amino-functionalized silica NPs ($\text{SiO}_2\text{-NH}_2$) show more affinity towards the bi-marker, since CEA is a protein heavily glycosylated that shows a negative global charge in physiological medium. The choice of using colloidal silica nanoparticles was related to a facile synthetic route, prone to adaptations and not requiring the use of toxic organic solvents.

The sol-gel method was optimized to produce spherical, uniform, porous and monodisperse silica nanoparticles of controllable size that were dispersed in water. Particle size depends on the concentration of reactants, catalysts and temperature. According to the literature, opposite to reaction time, reaction temperature is inversely related to the size of the nanoparticles [44].

Figure 16 portrays SEM images of the $\text{SiO}_2\text{-NH}_2$ NPs that were taken to verify their morphology and dispersion. Figure 16a,b show that the $\text{SiO}_2\text{-NH}_2$ NPs are arranged in large

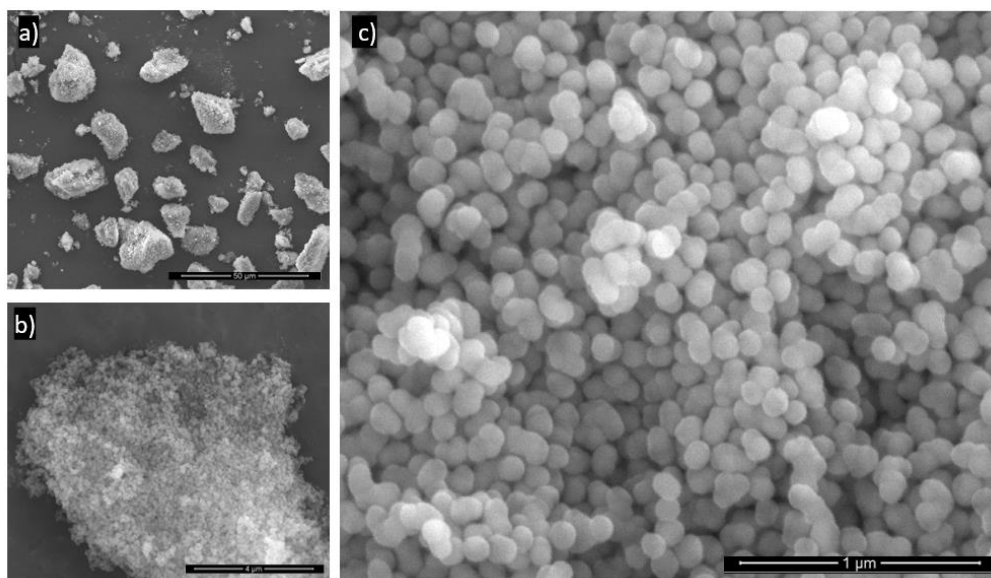


Figure 16: SEM images of powdered $\text{SiO}_2\text{-NH}_2$ NPs: (a) 2000x zoom, (b) 25 000x zoom and (c) 100 000x zoom.

agglomerates, which may be explained by back-bonding of NH_2 functional groups to silanols on the particle surface with consequent reduction of electrostatic repulsion [51]. Nonetheless, from Figure 16c it can be stated that the nanoparticles present a very narrow size distribution with a mean diameter of 172 ± 9 nm ($n=25$), further confirmed in the silica opal films (below in Figure 22a).

FTIR was used to confirm the presence of the amino groups on the surface of the silica nanoparticles, since its analysis allows identifying functional groups of samples. Figure 17 shows the FTIR spectra of silica nanoparticles synthesized without and with APTES in the formulation.

Digital Fabrication of Transparent Electrodes for Simultaneously Optical and Electrochemical Biosensor Applications

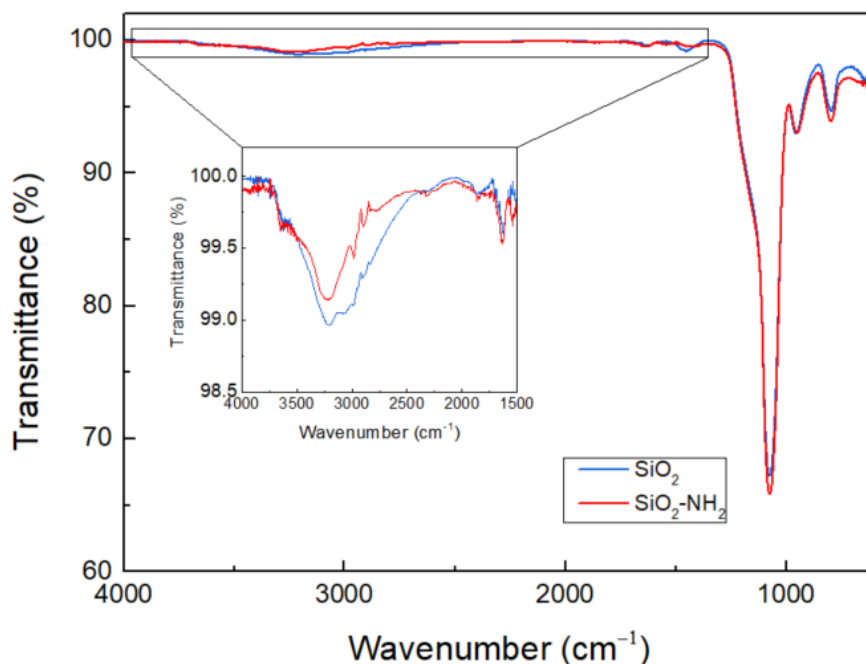


Figure 17: FTIR spectra of silica NPs with and without amino functionalization. The inset graph corresponds to a magnification of the spectra between 4000 cm⁻¹ and 1500 cm⁻¹.

Both spectra present similar features: the intense peak at 1074 cm⁻¹ can be associated with the asymmetric stretching vibrations of Si–O–Si with a shoulder around 1200 cm⁻¹. Also related to symmetric Si–O–Si stretching vibrations are the bands found around 955 cm⁻¹ and 795 cm⁻¹ [52]. The broad band present around 2500–3600 cm⁻¹ accounts for the Si–OH stretching vibrations [44]. Then, comparing the spectra from both types of NPs, some differences can be observed. The amino modified NPs show a weak band at 1526 cm⁻¹ justified by the N–H vibrations of the –NH₂ groups and also at 2988 cm⁻¹ and 2900 cm⁻¹ assigned to C–H vibrations of the –CH₂ groups [42]. Overall, it can be concluded that the functionalization with amine groups from APTES was effective.

3.3 Biosensor Construction

Before the construction of MIP materials, several parameters and conditions needed to be studied and adjusted. Therefore, the first steps are considered optimization of experimental variables. It must be remarked that pH is also a very important parameter, but it was always kept equal to 7.4 by using PBS buffer in all experiments, for being a similar value to biological fluids.

3.3.1 ITO Coated Glass Electrodes Characterization

Prior to the construction of the biosensors, clean ITO coated glass electrodes that act as substrates were electrochemically analyzed. The general behavior and properties of the WE were studied by several assays with the chosen redox probe solution and the results allowed to identify reference values to compare with the modifications of the subsequent construction steps.

Digital Fabrication of Transparent Electrodes for Simultaneously Optical and Electrochemical Biosensor Applications

After cleaning the electrodes as described in 2.5.2, CV and EIS scans were done, as shown in Figure 18. By interpreting the CV scan in Figure 18a, it is possible to identify oxidation and reduction peaks at -0.08 V and 0.1 V and from a current point of view, the system shows a *quasi*-reversible behavior, since the peaks currents are very similar, one being -0.10 mA and the other being 0.11 mA.

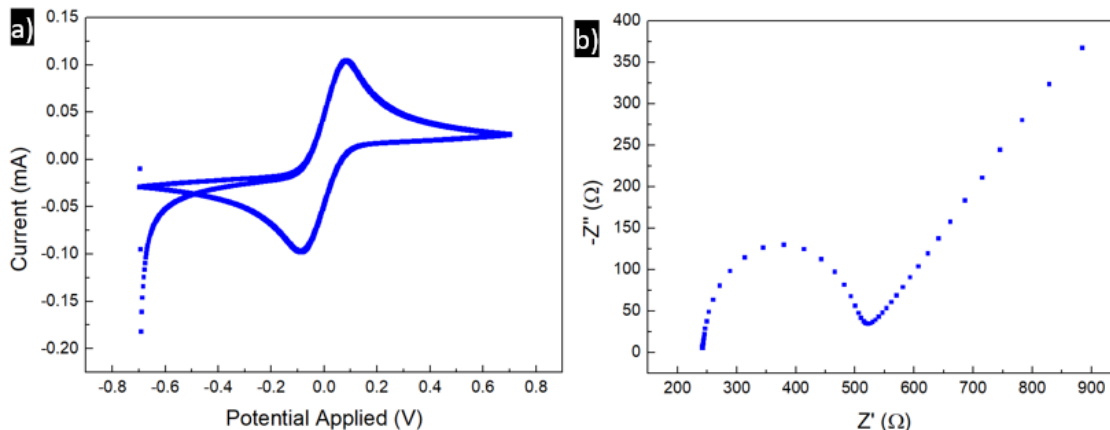


Figure 18: Electrochemical analysis of unmodified ITO coated glass electrodes: (a) CV and (b) EIS. The CV assay was performed from -0.7 V to 0.7 V (3 scans), with a scan rate of 50 mV/s and EIS was done with an amplitude of 0.01 V, with a logarithmic step type and a frequency range of 0.1 Hz to 0.1 MHz.

Peak separation is 180 mV, therefore the redox reaction of the clean ITO electrode is *quasi*-reversible, because a reversible reaction has only one electron involved in the reaction, making the expected value to be 59 mV. Figure 18b presents the EIS data that was fitted to the Randles equivalent circuit in order to extract the reference value of the charge transfer resistance, which is 259Ω .

3.3.2 Polymerization Conditions

Throughout the construction procedure of the biosensors, one of the most impactful stages in terms of electrochemical response is the electropolymerization of Py. Consequently, the effect of PPy on the ITO coated glass substrates must be studied and the first step is to identify the potential that is necessary to apply on the electrodes so that the Py oxidation occurs in the WE surface. This result is presented in Figure 19 and the graph shows that

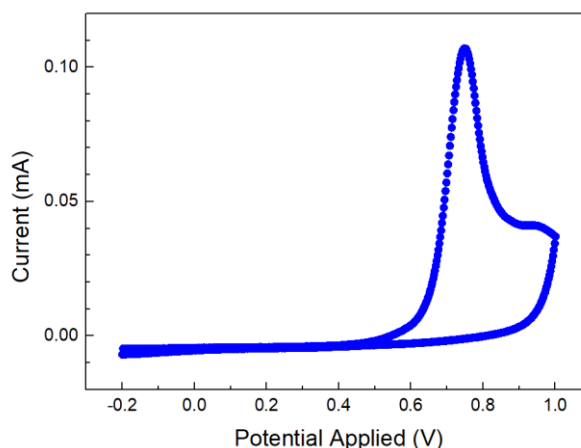


Figure 19: Study of the Py's oxidation potential. One CV scan was performed at 50 mV/s, from -0.2 V to 1 V.

Digital Fabrication of Transparent Electrodes for Simultaneously Optical and Electrochemical Biosensor Applications

an irreversible oxidation occurs between 0.58 V and 0.94 V, reaching its maximum at 0.75 V. This information allowed to choose an electropolymerization range from -0.2 V to 1 V that guarantees the polymerization of the monomer.

Monomer concentration is likewise one of the critical parameters, since it plays a major role in the conductivity of the polymer. Five different Py concentration values were tested: 10 mM, 30 mM, 50 mM, 70 mM and 90 mM. This study was done by electropolymerizing each concentration by performing 10 CV cycles at 50 mV/s and comparing the resulting EIS data of each experiment, as shown in Figure 20.

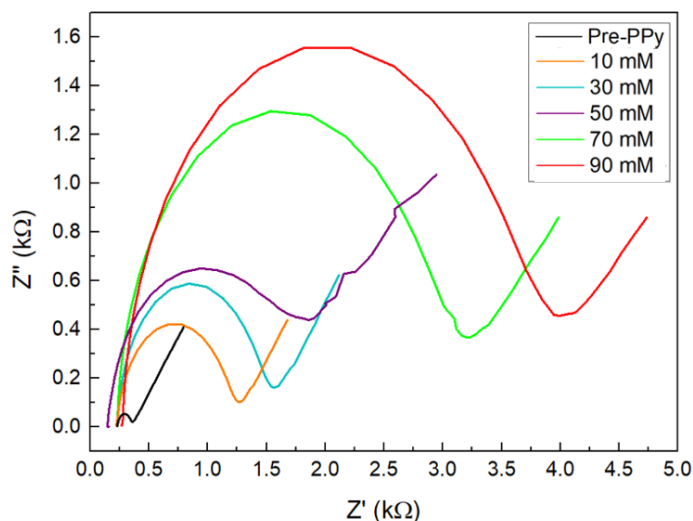


Figure 20: Comparison of EIS spectra of the resulting electropolymerization of different Py concentrations.

The spectra behavior is as expected, showing a proportional increase in R_{CT} as the monomer concentration rises and the biggest effect on conductivity is associated with the highest polymer concentration. Comparing the spectra with the one of cleaned ITO, serving as control, it is evident that all the electropolymerization attempts led to the formation of a polymeric film, considering that all concentrations present changes in the sensing surface. MIP materials present a challenge concerning the equilibrium between monomer concentration and distribution of recognition sites throughout the sensing surface. Thus, the decision surrounding the best concentration value relies on several parameters, such as the need of an intense measurable signal that proves the formation of PPy, the necessity of keeping a conductive interface and growing a polymeric layer with just enough thickness to guarantee a structure capable of integrating the NPs and creating proper imprinted cavities, without creating a diffusional barrier to allow a good sensor sensitivity. Taking all this into account, the concentration of 50 mM was chosen as optimal.

Along with monomer concentration, the number of electropolymerization cycles can have a significant effect, by controlling the film thickness and its structural properties. A large number of cycles produce a thicker polymeric layer and, consequently, it may lead to a less sensitive sensor due to a less conductive surface and possibly inhibiting the creation

Digital Fabrication of Transparent Electrodes for Simultaneously Optical and Electrochemical Biosensor Applications

of effective recognition sites. The CEA molecules may lay deep within the polymeric film surface, thus decreasing both the chances of a successful template removal as well as good subsequent recognition. On the other hand, a low number of cycles may not induce the formation of a PPy film with proper recognition cavities.

A study about the number of CV cycles was performed and a comparison was made between a chip before electropolymerization and chips where Py 50 mM was polymerized using 5 and 10 cycles, as depicted in Figure 21. Higher number of CV scans were assayed, but their EIS data was discarded due to lack of stabilization in the readings.

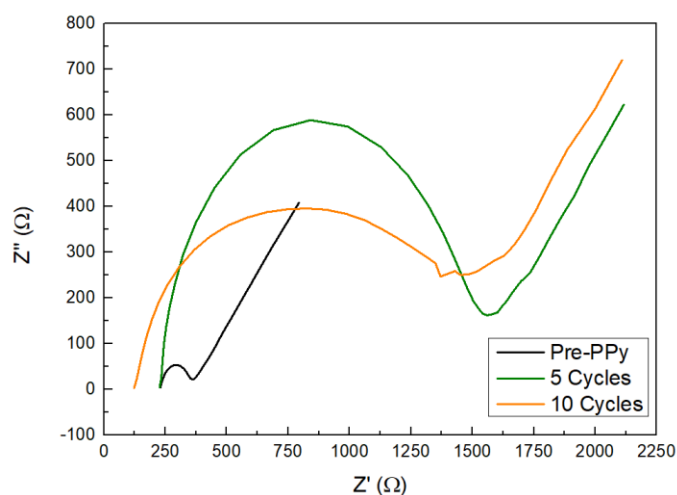


Figure 21: Comparison of EIS spectra of the resulting electropolymerization of Py 50 mM with different CV cycles.

By fitting the EIS spectra into a Randles equivalent circuit, it was assessed that the R_{CT} value for 5 and 10 cycles is 1220Ω and 1355Ω , respectively. So, 5 cycles was the chosen condition because it showed good stabilization and less resistivity when compared to 10 cycles, which will create a more penetrable matrix and therefore a more sensitive device.

Scan rate can also influence the stability and resistance of the created polymer, however a value of 50 mV/s was selected right away, since literature proved it to be the best in similar conditions to this type of application [32], [36]. These works performed a study to pick the best solvent to remove the protein after the polymerization stage without damaging the polymeric matrix. Based on those results, oxalic acid (0.5 M) was selected as it did not demonstrate significant interference with the WE surface [34, 36].

In conclusion, the best parameters for Py electropolymerization are a potential range going all the way to 1 V , such as from -0.2 V to 1 V , 50 mV/s of scan rate, 5 CV cycles and 50 mM of monomer concentration. The collection of these conditions allowed to successfully electropolymerize PPy films by an oxidative process, on the surface of an oxide layer.

3.3.3 Characterization of Sensor Assembly

The modified ITO WE was analyzed through SEM, to assess its morphology. These images are presented in Figure 22. Figure 22a portrays the obtained image of a transverse cut of vertical deposited $\text{SiO}_2\text{-NH}_2$ NPs on an ITO electrode where the same monodispersed, uniform and round particles from Figure 16 are visible, but now show consistent distribution, forming 15-20 layers, resulting in an extremely homogeneous surface.

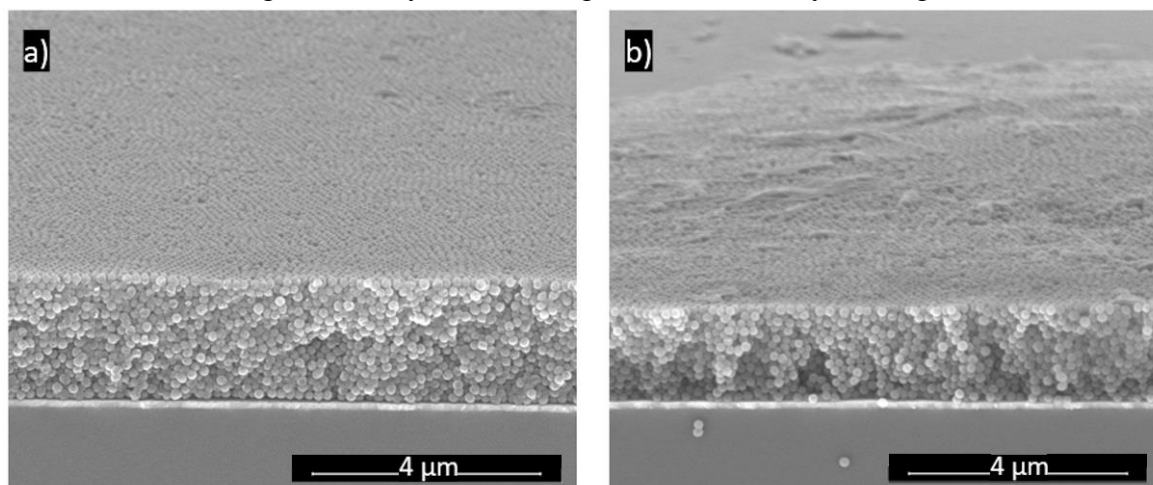


Figure 22: SEM images at 25000x zoom of (a) $\text{SiO}_2\text{-NH}_2$ NPs deposited on an ITO electrode, (b) PPy film electropolymerized by 5 CV cycles on a $\text{SiO}_2\text{-NH}_2$ NPs/ ITO electrode.

The formation of an opal structure is therefore confirmed. Figure 22b now shows the result of electropolymerizing Py (5 CV cycles) on the later surface. A lattice change due to polymer growth in the interstices of the assembled NPs is barely noticeable in the transverse section. On the other hand, the top layer is more irregular, suggesting the formation of polymer in the matrix.

Reflectance and EIS measurements were done along each stage of the biosensor assembly to validate each chemical modification done to the ITO electrode. The reflectance of the photonic crystal created by the nanostructured $\text{SiO}_2\text{-NH}_2$ NPs can be seen at the naked eye because it presents a blue color (Figure a). **Error! Reference source not found.** Figure b compares the reflectance spectra of ITO coated with PC, after PPy electropolymerization and after subsequent template removal, both in the case of MIP (with protein incubation) and in the NIP (control experiment).

Error! Reference source not found. Figure b displays the difference in reflectance in each modification step, where it can be observed that the reflectance of the PC created by the nanostructured NPs occurs around 330 nm and both NIP and MIP assembly processes may lead to a change in the refractive index and therefore a change in the reflectance intensity [53]. In this case, the presence of the target CEA molecules caused an increase in peak intensity when compared to the PC on ITO glass or to NIP. After template removal with oxalic acid, a significant decrease in reflectance is observed, suggesting an efficient template removal.

Digital Fabrication of Transparent Electrodes for Simultaneously Optical and Electrochemical Biosensor Applications

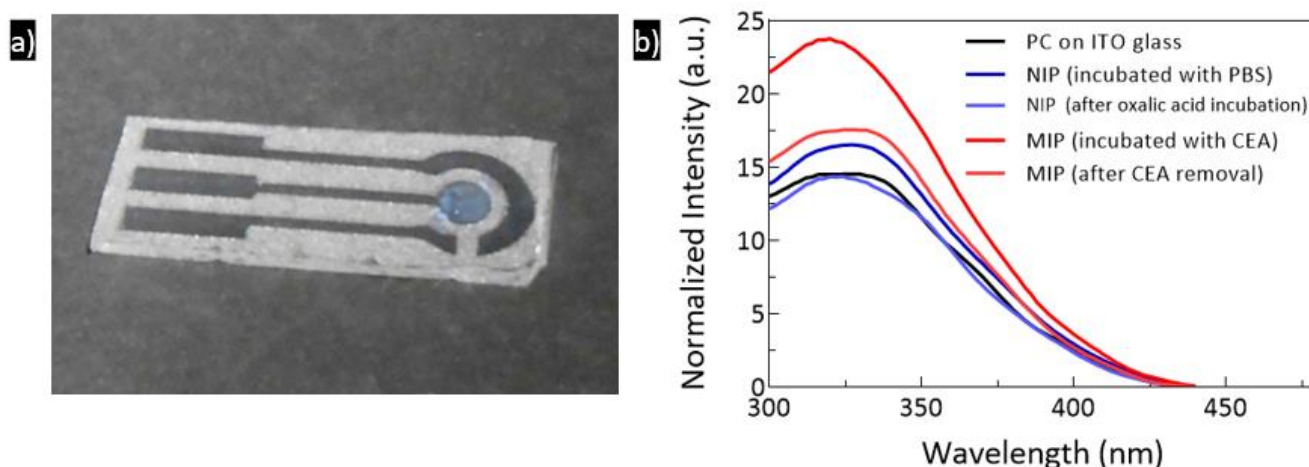


Figure 23: Photonic crystal assembled on the WE of the ITO electrode (a) and comparison of reflectance spectra of the different phases of construction of the MIP biosensor (b).

As expected, the EIS data obtained during sensor construction and depicted in Figure shows a great change between the original ITO surface and subsequent modifications. The increase in R_{CT} in the sample with silica NPs deposited on ITO is as expected, since the NPs create a barrier for the redox probe, therefore decreasing the conductivity of the created interface. From this figure, it can be observed that the ITO substrates before and after NPs deposition present a stable electrochemical response, with low resistances.

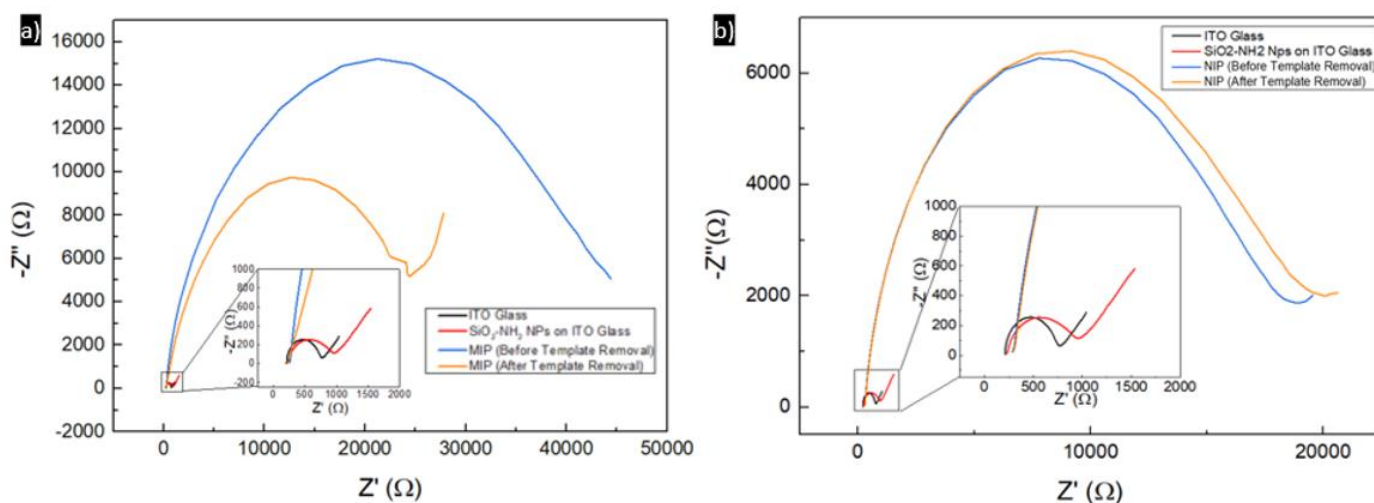


Figure 24: EIS responses of the different stages of MIP (a) and NIP (b) construction.

More than that, both MIP and NIP show higher resistance values after template incubation and polymer growth, considering the same conditions are applied with the only difference being the presence of CEA in MIP, which is responsible for the even higher resistance when compared to NIP. The increased resistance of the MIP and NIP samples is justified by the electropolymerization of Py. More PPy leads to higher resistivity, since the polymer shows an isolating behavior in these conditions and blocks electron transfer. As the polymer was growing by electropolymerization, the CEA molecules acted as template

Digital Fabrication of Transparent Electrodes for Simultaneously Optical and Electrochemical Biosensor Applications

and became entrapped within the polymeric matrix. After template removal, the NIP demonstrates a similar performance, since the matrix stays the same, as there is nothing to be chemically etched by the oxalic acid. In the MIP case, the oxalic acid successfully removes the template, leaving vacant recognition regions in the PPy matrix and leading to a decrease in the resistance. The removal of the template created vacant positions on the PPy film that have an analogous behavior to the interaction between antigens and antibodies, since they hold electrostatic and stereochemical complementary features towards CEA molecules. Both samples do not show a linear portion at lower frequencies on their Nyquist diagrams, therefore the diffusion process are insignificant or non-existent.

Overall, the combined information from electrochemical and optical measurements confirmed the successful formation of NIP and MIP films on the opal structured silica NPs. Sensor design is schematically shown in Figure 23.

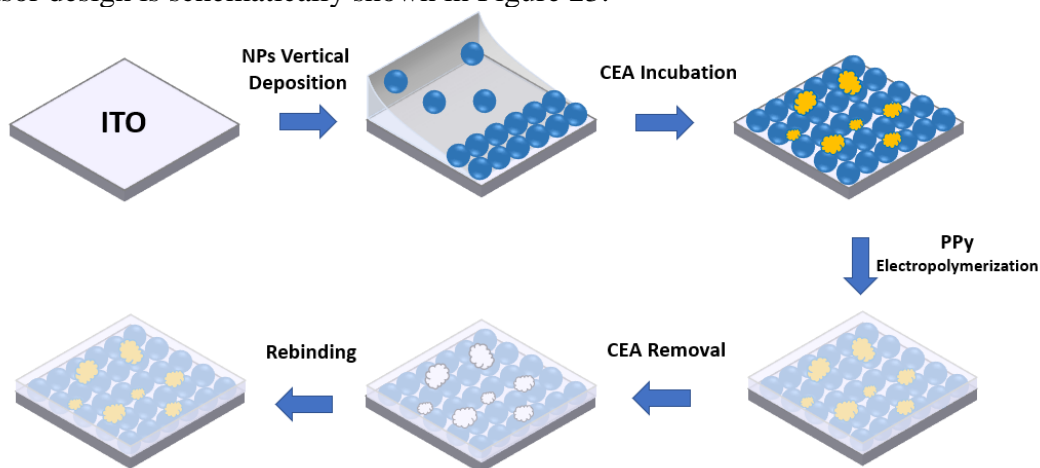


Figure 23: Schematic representation of the stages performed in the fabrication of MIP devices.

3.4 Performance of MIP Sensor

3.4.1 Calibration Curves

The analytical performances of the CEA biosensor, both electrochemical and optical, were assessed by recording calibration curves. The purpose is to demonstrate the ability of the sensor to recognize the target biomarker, relying on the high affinity recognition cavities in the MIP materials. After assembly and before calibrations, each device was incubated in PBS buffer for the attaining of a stable response. Afterwards, CEA concentrations were incubated for 40 minutes each and the electrochemical response of the MIP sensor was followed by EIS assays. The NIP was simultaneously evaluated. Optical performance was simultaneously measured by carrying out reflectance measurements at the end of each electrochemical assay.

Digital Fabrication of Transparent Electrodes for Simultaneously Optical and Electrochemical Biosensor Applications

Sensor response to increasing concentrations of CEA (1, 2.5, 5 and 10 ng/mL) was followed both through EIS (Figure 24) and reflectance (Figure 25) measurements, for electrochemical and optical detection, respectively.

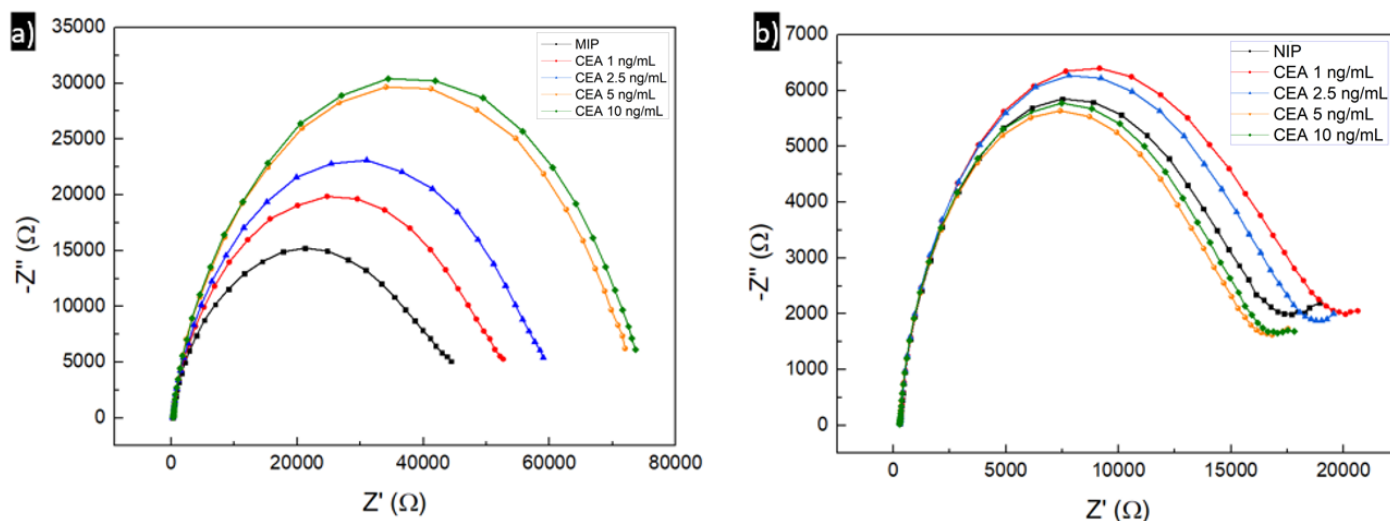


Figure 24: EIS spectra of the biosensor calibration procedure for MIP (a) and NIP (b) devices.

Figure 24a shows the obtained EIS results for the MIP, portraying an increase of resistance of the sensing layer after incubation with CEA solutions. This resistance increment is justified by the rebinding of CEA into the imprinted cavities in the polymer thus creating an additional barrier for the redox probe to access the electrode surface. As more biomarker molecules are trapped in the biosensing matrix, less electrons are transferred, increasing the diameter of the Nyquist semicircles. The NIP sensor displayed a very different performance, not showing any response towards the increment in CEA concentration, since the only interactions between the NIP and the biomarker molecules are non-specific, such as surface adsorption, which are not enough for an electrochemical significant response.

As increasing concentrations of CEA are specifically recognized by the imprinted polymer embedding the PC, the main response observed is a gradually increase in the reflectance peak intensity (Figure 25a), suggesting changes in the lattice or average refractive index [54].

The same calibration study was done simultaneously to a NIP, produced under the same conditions but with the absence of CEA template. From Figure 25b, it is observed that the NIP shows some changes at each calibration step. Nonetheless, the intensities vary within a small range and the response is not linear with the increase of CEA concentration. NIP materials do not have recognition sites, since they were not produced with a template, so the observed changes in reflectance are associated with non-specific molecular adsorption of CEA to the polymer's surface.

Digital Fabrication of Transparent Electrodes for Simultaneously Optical and Electrochemical Biosensor Applications

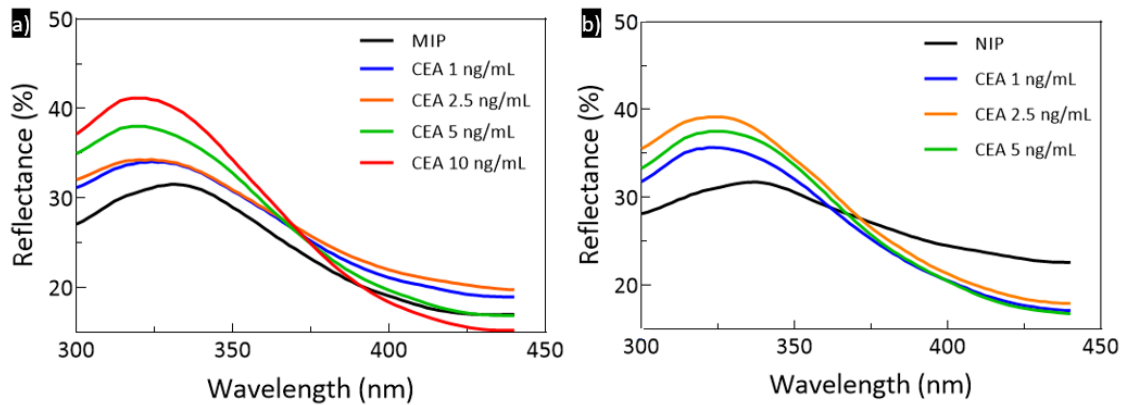


Figure 25: Optical responses of MIP (a) and NIP (b) biosensors to different CEA concentrations.

From these spectra, R_{CT} values were taken and processed in function of CEA concentration, as demonstrated in Figure 26. The calibration curve for the NIP sensor shows a re-

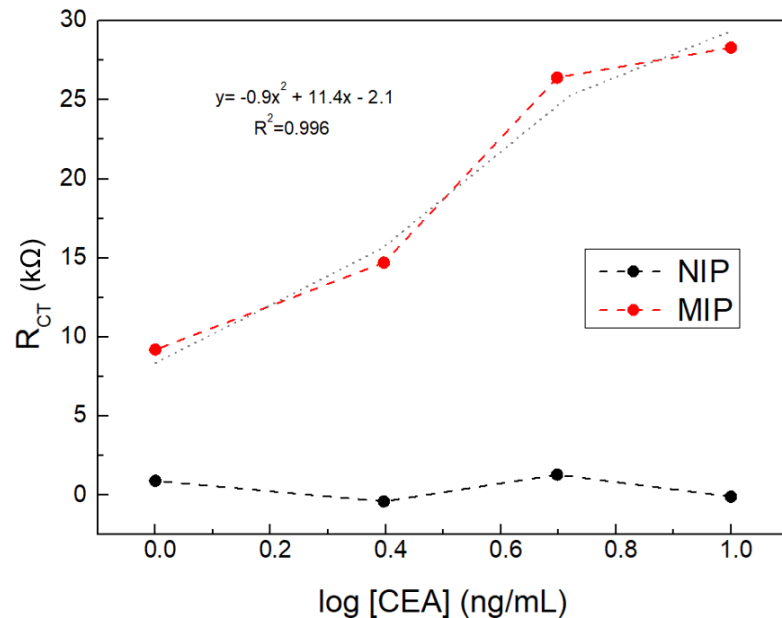


Figure 26: Calibration curves of MIP and NIP based biosensors obtained by EIS measurements with increasing CEA concentration.

ponse independent of the CEA concentration, presenting very low random values, proving to be a good control material. As for the MIP sensor, the calibration curve has an almost linear behavior, but more data points were needed to prove this, as a linear fit had a squared correlation coefficient of only 0.94. With the acquired results, the best fit was a polynomial equation of second degree that had a R^2 of 0.996, proving that further studies are needed to achieve a fully linear response to the CEA concentration. Nonetheless, the MIP based sensor shows a good sensitivity, being able to recognize even the lowest CEA concentration, which is a good indicator of a promising technology.

Digital Fabrication of Transparent Electrodes for Simultaneously Optical and Electrochemical Biosensor Applications

Figure 27 summarizes the calibration curves obtained through the optical analysis. Optically, the MIP shows an almost linear behavior and the NIP presented random peak intensities with increasing concentrations of CEA, a trend very similar to the electrochemical response. Considering MIP response, a linear fit could be achieved with a R^2 of 0.997, if the first data point is disregarded, otherwise the obtained results would be represented by a complex polynomial equation of second degree. Higher concentrations lead to higher values of reflectance, although these changes are still not visible at the naked eye by a color gradient. More studies must be conducted to guarantee an absolute linear response and, ideally, a gradual shift in color capable of being detected by the naked eye.

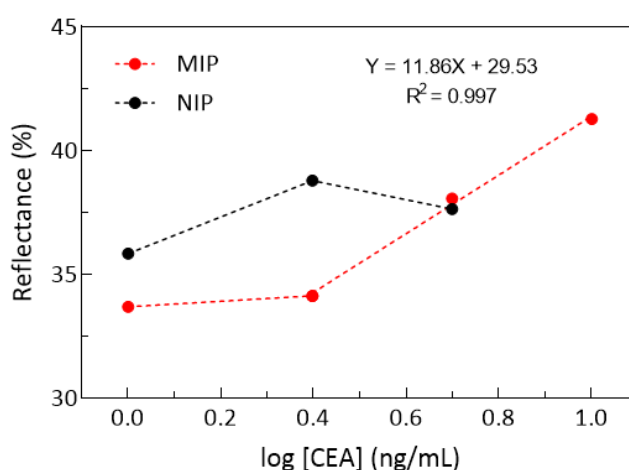


Figure 27: Calibration curves of MIP and NIP devices obtained by reflectance analysis in function of CEA concentration.

MIP-based biosensors show a good response to low concentrations of CEA, but due to lack of replicated data, further optimizations are still needed.

4 | Conclusion

In this dissertation, the deposition of AZO thin films by RF magnetron sputtering was optimized first to evaluate if an ITO replacement could present similar electrical and optical properties. It was found that a post-deposition thermal treatment significantly affects structural, optical, and electrical properties of AZO films. Low resistivity and high transparency can be achieved by adjusting the substrate deposition parameters of Al-doped ZnO thin films. The best conditions were a balance between transmittance of AZO films, which was about 80 % in the visible range and the minimum resistivity reached, which was 129.7 $\mu\Omega\cdot\text{cm}$ at a deposition done at 100 W, thermally treated at 500 °C.

The second half of this thesis was the application of TCO's to fabricate a biosensor with dual recognition applied to CEA detection. The functionalized colloidal silica nanoparticles proved to be a great choice as template to produce a photonic opal structure. This material may be easily functionalized and shows a large surface area, making it easier to tune the interactions with the target molecules. Moreover, the self-assembly by vertical deposition showed to be a straightforward approach to develop a photonic crystal based-sensor.

The molecularly imprinted polymers have a good response to low concentrations of target molecule, confirming a successful entrapment and formation of imprinted cavity sites. This technology offers several advantages, namely the possibility to tailor a polymer to recognize a desired biomarker, avoiding the use of expensive natural antibodies and therefore reducing the production costs. The use of laser direct writing for the electrode patterning, also lowers the biosensors price, as it replaces several lengthy fabrication steps and the need of masks for a fast and precise method. Overall, the proposed biosensor proved to be a promising simple and point-of-care tool to achieve the early diagnosis of cancer.

Electrochemical and optical biosensing devices based on MIP have gotten great attention in the past two decades, contrary to devices based on dual-mode recognition techniques, which have been surprisingly ignored. Thus, the proposed biosensor is state of the art by combining optical and electrochemical sensing, which provides unique insight into the monitoring and detection of biomolecules and merging it with the technology of molecularly imprinted polymers.

Future perspectives are to repeat optical and EIS assays to decrease the limit of detection of the biosensors and to try a wider range of CEA concentrations to improve its linear response, followed by selectivity tests and trials with real human samples. The application of the optimized AZO thin films for biosensing would also be of great interest, considering it could even be used with flexible substrates.

Future challenges in the field, in general, are to guarantee reproducibility and to enhance sensitivity and selectivity to a point where industrial applications can be considered. Several steps could also be optimized to be more easily applicable to large-scale processes,

Digital Fabrication of Transparent Electrodes for Simultaneously Optical and Electrochemical Biosensor Applications

such as switching the colloidal self-assembly of silica nanoparticles by a spin coating deposition.

References

- [1] Eurostat, “Cancer Statistics,” 2017. [Online]. Available: https://ec.europa.eu/eurostat/statistics-explained/index.php?title=Cancer_statistics#Further_Eurostat_information. [Accessed: 30-Jul-2018].
- [2] E. NIEDERLAENDER, “Causes of death in the EU,” 2006.
- [3] E. E. Yörüker, S. Holdenrieder, and U. Gezer, “Blood-based biomarkers for diagnosis, prognosis and treatment of colorectal cancer,” *Clin. Chim. Acta*, vol. 455, pp. 26–32, 2016.
- [4] M. J. Selleck, M. Senthil, and N. R. Wall, “Making Meaningful Clinical Use of Biomarkers,” *Biomark. Insights*, vol. 12, pp. 1–7, 2017.
- [5] I. A. Umelo, B. Costanza, and V. Castronovo, “Innovative methods for biomarker discovery in the evaluation and development of cancer precision therapies,” *Cancer Metastasis Rev.*, vol. 37, no. 1, pp. 125–145, 2018.
- [6] F. Ye, Y. Zhao, R. El-Sayed, M. Muhammed, and M. Hassan, “Advances in nanotechnology for cancer biomarkers,” *Nano Today*, vol. 18, pp. 103–123, 2018.
- [7] J. Nan, J. Li, X. Li, G. Guo, X. Wen, and Y. Tian, “Preoperative Serum Carcinoembryonic Antigen as a Marker for Predicting the Outcome of Three Cancers,” *Biomark. Cancer*, vol. 9, pp. 1–7, 2017.
- [8] S.-Y. Zhang, M. Lin, and H.-B. Zhang, “Diagnostic value of carcinoembryonic antigen and carcinoma antigen 19-9 for colorectal carcinoma,” *Int. J. Clin. Exp. Pathol.*, vol. 8, no. 8, pp. 9404–9, 2015.
- [9] M. J. Duffy, “Carcinoembryonic antigen as a marker for colorectal cancer: Is it clinically useful?,” *Clin. Chem.*, vol. 47, no. 4, pp. 624–630, 2001.
- [10] N. Gan, L. Jia, and L. Zheng, “A sandwich electrochemical immunosensor using magnetic DNA nanoprobe for carcinoembryonic antigen,” *Int. J. Mol. Sci.*, vol. 12, no. 11, pp. 7410–7423, 2011.
- [11] K. L. Zakian, A. Shukla-Dave, E. Ackerstaff, H. Hricak, and J. a Koutcher, “¹H magnetic resonance spectroscopy of prostate cancer: biomarkers for tumor characterization,” *Cancer Biomark.*, vol. 4, no. 4–5, pp. 263–276, 2008.
- [12] T. M. H. Lee, “Over-the-counter biosensors: Past, present, and future,” *Sensors*, vol. 8, no. 9, pp. 5535–5559, 2008.
- [13] P. Damborsky, J. vitel, and J. Katrlík, “Optical biosensors,” *Essays Biochem.*, vol. 60, no. 1, pp. 91–100, 2016.
- [14] G. Zanchetta, R. Lanfranco, F. Giavazzi, T. Bellini, and M. Buscaglia, “Emerging applications of label-free optical biosensors,” *Nanophotonics*, vol. 6, no. 4, pp. 627–645, 2017.
- [15] X. Fan, I. M. White, S. I. Shopova, H. Zhu, J. D. Suter, and Y. Sun, “Sensitive optical biosensors for unlabeled targets: A review,” *Anal. Chim. Acta*, vol. 620, no. 1–2, pp. 8–26, 2008.
- [16] U. D. H. Inan, M. Poyraz, F. Inci, M. A. Lifson, M. Baday, B. T. Cunningham, “Photonic crystals: emerging biosensors and their promise for point-of-care

- applications,” vol. 46, no. 2, pp. 366–388, 2017.
- [17] G. I. N. Waterhouse and M. R. Waterland, “Opal and inverse opal photonic crystals: Fabrication and characterization,” *Polyhedron*, vol. 26, no. 2, pp. 356–368, 2007.
- [18] A. Di Falco, L. O’Faolain, and T. F. Krauss, “Photonic crystal slotted slab waveguides,” *Photonics Nanostructures - Fundam. Appl.*, vol. 6, no. 1, pp. 38–41, 2008.
- [19] L. Nucara, F. Greco, and V. Mattoli, “Electrically responsive photonic crystals: A review,” *J. Mater. Chem. C*, vol. 3, no. 33, pp. 8449–8467, 2015.
- [20] C. López, “Materials Aspects of Photonic Crystals,” *Adv. Mater.*, vol. 15, no. 20, pp. 1679–1704, 2003.
- [21] P. N. Patel, V. Mishra, and A. S. Mandloi, “Optical Biosensors : Fundamentals & Trends,” *J. Eng. Res. Stud.*, vol. I, no. I, pp. 15–34, 2010.
- [22] S. H. Kim, S. Y. Lee, S. M. Yang, and G. R. Yi, “Self-assembled colloidal structures for photonics,” *NPG Asia Mater.*, vol. 3, no. 1, pp. 25–33, 2011.
- [23] Christopher M A Brett; Ana Maria Oliveira Brett, “Electrochemistry : principles, methods, and applications,” vol. 98, 1996, p. 48324.
- [24] Z. Samec, E. Samcová, and H. H. Girault, “Ion amperometry at the interface between two immiscible electrolyte solutions in view of realizing the amperometric ion-selective electrode,” *Talanta*, vol. 63, no. 1, pp. 21–32, 2004.
- [25] C. Mousty, “Sensors and biosensors based on clay-modified electrodes - New trends,” *Appl. Clay Sci.*, vol. 27, no. 3–4, pp. 159–177, 2004.
- [26] D. Grieshaber, R. MacKenzie, J. Vörös, and E. Reimhult, “Electrochemical biosensors - Sensor principles and architectures,” *Sensors*, vol. 8, no. 3, pp. 1400–1458, 2008.
- [27] E. H. Yoo and S. Y. Lee, “Glucose biosensors: An overview of use in clinical practice,” *Sensors*, vol. 10, no. 5, pp. 4558–4576, 2010.
- [28] J. Erdo(double acute)ssy, V. Horváth, A. Yarman, F. W. Scheller, and R. E. Gyurcsányi, “Electrosynthesized molecularly imprinted polymers for protein recognition,” *TrAC - Trends Anal. Chem.*, vol. 79, pp. 179–190, 2016.
- [29] M. I. Prodromidis, “Impedimetric immunosensors-A review,” *Electrochim. Acta*, vol. 55, no. 14, pp. 4227–4233, 2010.
- [30] T. P. Nguy, T. Van Phi, D. T. N. Tram, K. Eersels, P. Wagner, and T. T. N. Lien, “Development of an impedimetric sensor for the label-free detection of the amino acid sarcosine with molecularly imprinted polymer receptors,” *Sensors Actuators, B Chem.*, vol. 246, pp. 461–470, 2017.
- [31] G. V. Martins, A. C. Marques, E. Fortunato, and M. G. F. Sales, “8-hydroxy-2'-deoxyguanosine (8-OHdG) biomarker detection down to piconMolar level on a plastic antibody film,” *Biosens. Bioelectron.*, 2016.
- [32] F. T. C. Moreira, M. J. M. S. Ferreira, J. R. T. Puga, and M. G. F. Sales, “Screen-printed electrode produced by printed-circuit board technology. Application to cancer biomarker detection by means of plastic antibody as sensing material,” *Sensors Actuators, B Chem.*, vol. 223, pp. 927–935, 2016.
- [33] B. T. S. B. Karsten Haupt, Ana V. Linares, Marc Bompert, “Molecularly Imprinted

- Polymers,” *Top Curr Chem*, vol. 325, no. 1, pp. 1–28, 2012.
- [34] A. R. Cardoso, A. P. M. Tavares, and M. G. F. Sales, “In-situ generated molecularly imprinted material for chloramphenicol electrochemical sensing in waters down to the nanomolar level,” *Sensors Actuators, B Chem.*, vol. 256, pp. 420–428, 2018.
- [35] H. R. Culver and N. A. Peppas, “Protein-Imprinted Polymers: The Shape of Things to Come?,” *Chem. Mater.*, vol. 29, no. 14, pp. 5753–5761, 2017.
- [36] M. L. Gonçalves, “Desenvolvimento de um biossensor para rápido diagnóstico da doença de Alzheimer,” 2016.
- [37] E. Fortunato, P. Barquinha, and R. Martins, “Oxide semiconductor thin-film transistors: A review of recent advances,” *Adv. Mater.*, vol. 24, no. 22, pp. 2945–2986, 2012.
- [38] E. Fortunato, D. Ginley, H. Hosono, and D. C. Paine, “Transparent Conducting Oxides for Photovoltaics,” *MRS Bull.*, vol. 32, no. 3, pp. 242–247, 2007.
- [39] P. Tang, B. Li, and L. Feng, “The optical and electrical properties of ZnO:Al thin films deposited at low temperatures by RF magnetron sputtering,” *Ceram. Int.*, no. November, 2017.
- [40] K. K. Kim *et al.*, “Effect of rapid thermal annealing on Al doped n-ZnO films grown by RF-magnetron sputtering,” *Japanese J. Appl. Physics, Part 1 Regul. Pap. Short Notes Rev. Pap.*, vol. 44, no. 7 A, pp. 4776–4779, 2005.
- [41] S.-Y. Kuo *et al.*, “Effects of RF power on the structural, optical and electrical properties of Al-doped zinc oxide films,” *Microelectron. Reliab.*, vol. 50, no. 5, pp. 730–733, 2010.
- [42] W. MacDonald *et al.*, “Latest advances in substrates for flexible electronics,” *J. SID*, *J. Sid*, vol. 15, no. 12, p. 1075, 2007.
- [43] Y. Han *et al.*, “Unraveling the Growth Mechanism of Silica Particles in the Stober Method: In Situ Seeded Growth Model,” *Langmuir*, vol. 33, no. 23, pp. 5879–5890, 2017.
- [44] A. Y. Kardys, D. J. Bharali, and S. A. Mousa, “Amino-functionalized silica nanoparticles: In vitro evaluation for targeted delivery and therapy of pancreatic cancer,” *J. Nanotechnol.*, vol. 2013, 2013.
- [45] A. M. Jakob and T. A. Schmedake, “A novel approach to monodisperse, luminescent silica spheres,” *Chem. Mater.*, vol. 18, no. 14, pp. 3173–3175, 2006.
- [46] A. Lyubchik *et al.*, “Influence of post-deposition annealing on electrical and optical properties of ZnO-based TCOs deposited at room temperature,” *Phys. Status Solidi Appl. Mater. Sci.*, vol. 213, no. 9, pp. 2317–2328, 2016.
- [47] K. H. Patel and S. K. Rawal, “Influence of power and temperature on properties of sputtered AZO films,” *Thin Solid Films*, pp. 6–11, 2016.
- [48] G. P. Gonçalves, “Filmes finos de óxido de índio e zinco e sua aplicação em díodos orgânicos emissores de luz,” p. 6, 2011.
- [49] H. Kim *et al.*, “Electrical, optical, and structural properties of indium-tin-oxide thin films for organic light-emitting devices,” *J. Appl. Phys.*, vol. 86, no. 11, pp. 6451–6461, 1999.
- [50] J. Wang, A. Sugawara-Narutaki, M. Fukao, T. Yokoi, A. Shimojima, and T.

Digital Fabrication of Transparent Electrodes for Simultaneously Optical and
Electrochemical Biosensor Applications

- Okubo, “Two-phase synthesis of monodisperse silica nanospheres with amines or ammonia catalyst and their controlled self-assembly,” *ACS Appl. Mater. Interfaces*, vol. 3, no. 5, pp. 1538–1544, 2011.
- [51] R. P. Bagwe, L. R. Hilliard, and W. Tan, “Surface Modification of Silica Nanoparticles to Reduce Aggregation and Nonspecific Binding,” *Langmuir*, vol. 22, no. 9, pp. 4357–4362, 2006.
- [52] R. Scaffaro, L. Botta, G. Lo Re, R. Bertani, R. Milani, and A. Sassi, “Surface modification of poly(ethylene-co-acrylic acid) with amino-functionalized silica nanoparticles,” *J. Mater. Chem.*, vol. 21, no. 11, pp. 3849–3857, 2011.
- [53] C. Guo *et al.*, “Detection of bisphenol A using an opal photonic crystal sensor,” *Sensors Actuators, B Chem.*, vol. 166–167, pp. 17–23, 2012.
- [54] X. Hong *et al.*, “A novel opal closest-packing photonic crystal for naked-eye glucose detection,” *Small*, vol. 10, no. 7, pp. 1308–1313, 2014.

Digital Fabrication of Transparent Electrodes for Simultaneously Optical and Electrochemical Biosensor Applications

Appendix A

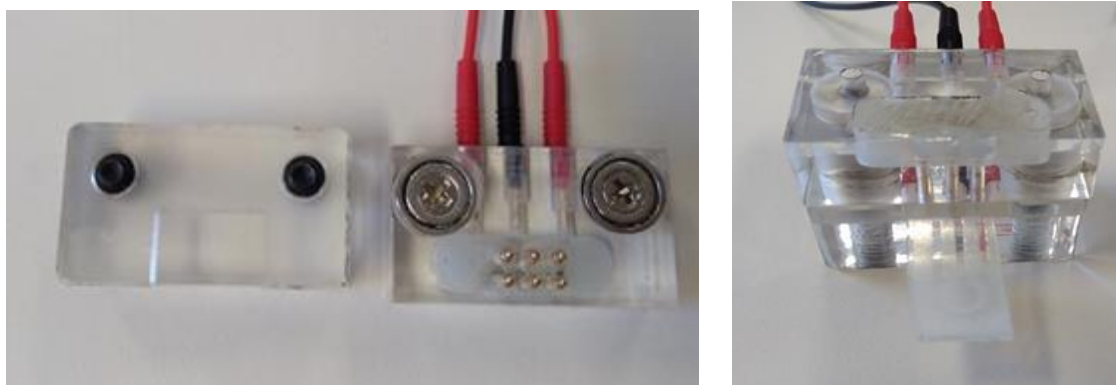


Figure A.0. 1: Homemade interface between the potentiostat and the electrodes.

The device presented in Figure A.0. 1 was used to read glass substrate electrodes, since the DropSens accessory was not able to fit them. The body of the interface is made out of acrylic, which was cut using the Universal Laser System CO2 VLS 3.5 available at CENIMAT, at full power. The top half contains three sockets to attach the cables that connect to the potentiostat along with six gold spring loaded pins that act as contacts, acquired from RS Components. The bottom half has a laser eroded cavity to support the electrodes, as well as two magnets to link both halves together. The spring loaded pins were 1mm apart, following the design of the used electrodes. Every perforation was mechanically created with a small drill.